

Politecnico di Torino

Master's Degree in Electronic Engineering



Master's Degree Thesis

**Advanced Materials for the Fabrication of
Innovative Micro-Supercapacitors:
optimization of laser-induced graphene on
polymeric substrates**

Supervisor: Prof. Andrea Lamberti

Candidate name: Ye Tian

October 2021

Abstract

Researchers have recently begun to study lower-cost graphene preparation methods easy to be scaled up. Among them, laser writing allows a fast photothermal conversion of some polymeric substrates (e.g., polyimide) into porous conductive path of few-layer graphene known as Laser Induced Graphene (LIG). Due to high electrical conductivity and the simple and fast fabrication procedure we focus on LIG for the fabrication of micro supercapacitors. Supercapacitors are kind of electrochemical energy storage devices which are based on carbon nano materials. Here we report on the optimization of the laser parameter in order to produce and pattern porous graphene-like films on polyimide by absorbing the CO₂ infrared laser energy and converting polyimide surface into graphene network. Indeed, noticed several important parameters of the laser (raster, power, frequency, velocity) affect the resistance of samples measured by means of Van der Pauw method. As we know, the performance of a supercapacitor can be characterized by a series of key parameters, including the cell capacitance, operating voltage, equivalent series resistance, power density, energy density and time constant. Therefore, the aim of this work is to minimize sheet resistance to improve performance of LIG-based supercapacitors, and optimize electrodes area (charge balance approach) in order to maximize the operating voltage of the devices. In this thesis work, we exploited two different setups: one is two-electrodes configuration for device characterization and the other one is the three-electrodes configuration fabricated to optimize the electrochemical energy storage of the final device. Electrochemical methods were exploited to characterize and optimize the devices: cyclic voltammetry (CV), electrochemical impedance spectroscopy (EIS), Galvanostatic charge and discharge (GCD). We compared performance of three-electrodes system with two different room temperature ionic liquids (ILs), such as ([EMIM][TFSI] and [PYR14][TFSI],) through analyzing and comparing areal capacitance, coulombic efficiency and so on. The conclusion is that [PYR14][TFSI] has larger stability window. Out of three electrodes measurements we derived an information concerning the

asymmetry factor between the electrodes. Finally, we tested stability of new devices printed with new masks by charge and discharge for long cycles. In summary, LIG-based supercapacitors with charge balancing show extremely high stability when compared to unbalanced ones.

Content

Chapter 1 Introduction	8
1.1 Supercapacitors	8
1.2 Micro supercapacitors	11
1.2.1 Application of micro supercapacitors	12
1.3 Graphene	13
1.3.1 Application of graphene in supercapacitors	14
1.3.2 Laser-induced graphene supercapacitors.....	15
1.4 The effect of electrode impedance on supercapacitors.....	17
1.5 Electrolytes.....	19
1.5.1 Aqueous electrolyte	20
1.5.2 Organic electrolyte	21
1.5.3 Ionic liquid electrolyte	22
Chapter 2 Laser parameters.....	24
2.1 Van der Pauw method.....	24
2.2 Laser parameters effects the impedance of graphene.....	25
Chapter 3 The device design	32
3.1 three-electrode system.....	32
3.2 Preparation and assembly.....	34
3.3 Main performance indicators of supercapacitors	36
3.4 Electrochemical performance evaluation techniques	40
3.5 Aim of study	47
Chapter 4 Experimental.....	49

4.1 Comparison between [EMIM][TFSI] and [PYR14][TFSI]	49
4.2 Comparison of different devices using [PYR14][TFSI]	51
4.3 Oxygen effect on [PYR14][TFSI]	53
4.4 Select the most appropriate laser parameters	56
4.5 Optimize charge balancing	60
4.5.1 Redesign masks	62
4.5.2 Results	68
Chapter 5 Conclusions	71
Bibliography	72

List of Figures

Figure 1.1 Structure of supercapacitor	10
Figure 1.2 Graphene structure formed by carbon atoms.....	13
Figure 1.3 LIG	17
Figure 1.4 The equivalent circuit of supercapacitor	18
Figure 1.5 Classification of electrolytes for electrochemical supercapacitors	20
Figure 2.1 The design of Van der Pauw cross.....	24
Figure 2.2 LIG Van der Pauw crosses.....	26
Figure 2.3 Van der Pauw crosses covered with silver paste	27
Figure 2.4 The change of resistance with different laser parameters.....	30
Figure 3.1 The difference between three-electrode and two-electrode systems ..	32
Figure 3.2 The original mask and interdigitated LIG samples	33
Figure 3.3 A LIG sample assembled.....	35
Figure 3.4 Ragone plot.....	39
Figure 3.5 CVs at multiple scan rates	41
Figure 3.6 Anodic/cathodic test	43
Figure 3.7 Nyquist plot	44
Figure 3.8 A three-electrode cell.....	45
Figure 3.9 The change of voltage versus time	45
Figure 3.10 IR drop.....	46
Figure 3.11 Float test	47
Figure 4.1 The structure of the two different ILs.....	50
Figure 4.2 Electrochemical performance of two different ILs.....	51
Figure 4.3 Electrochemical performance of three cells	52
Figure 4.4 Vacuum packaged [PYR14][TFSI].....	54
Figure 4.5 Electrochemical performance of new and old [PYR14][TFSI].....	55
Figure 4.6 Enlarged view of coulombic efficiency curve	56

Figure 4.7 The drift of counter electrode	57
Figure 4.8 Cyclic voltammetry under cathodic test	58
Figure 4.9 Electrochemical performance of four cells.....	59
Figure 4.10 Nyquist plot of four devices	60
Figure 4.11 Redesign masks in three ways	63
Figure 4.12 Laser cutting straight lines.....	64
Figure 4.13 The morphologies of laser-cutting straight line.....	65
Figure 4.14 The connection way of cell for GCD/float test	65
Figure 4.15 GCD test of three cells	66
Figure 4.16 Ragone plot of two cells	67
Figure 4.17 Seven new masks.....	68
Figure 4.18. Electrochemical behavior of eight cells	69
Figure 4.19 Float test of three cells.....	70

List of Tables

Table 2.1 Experimental laser parameters	28
Table 4.1 Tested cells	49
Table 4.2 The equivalent capacitance	60
Table 4.3 Experimental laser-cutting parameters.....	64

Chapter 1 Introduction

The continual rise of the worldwide population, along with the fast development of the global economy, has resulted in a surge in energy consumption. Over-exploitation and usage of fossil fuels like petroleum and coal have resulted in severe energy shortages and pollution. As a result, with the continuous strategic adjustment of the energy structure, the proportion of fossil energy will be gradually reduced in the future. The creation of new green renewable energy has become the most common problem and research hotspot in the world today. In recent decades, some clean energy sources, such as wind energy, tidal energy, solar energy, and hydrogen energy, have been developed and applied one after another, making essential contributions to alleviating the energy crisis and reducing environmental pollution. New and clean energy is occupying an increasingly important position in the world. At the same time, to solve various problems in new green energy and energy utilization, the development of new high-capacity energy storage equipment has become a high-tech competition in the world. Among them, lithium-Ion batteries and supercapacitors are typical representatives of current new energy technologies.

1.1 Supercapacitors

Energy storage equipment can be divided according to energy and power densities [1]. As a power-type energy storage device, supercapacitors are energy storage devices between traditional capacitors and batteries. It fills the gap between traditional electrostatic capacitors (high power density, low energy density) and batteries (high energy density, low power density) [2][3]. With the increasing attention on supercapacitors, more and more researchers have joined in the research and development of supercapacitors. If we look back at the development history of supercapacitors, we will find that supercapacitors have a history of more than 100 years

of development so far [4]. In 1879, Helmholtz firstly described the phenomenon of an electric double layer at the interface and proposed an explanatory model for the plate capacitor[3]. In 1957, the scientist Becker used the principle of an electric double layer to store charge, made a breakthrough in the fabrication of supercapacitors [5].

Supercapacitors have been developed rapidly in recent years and are widely used in the fields of electronic device, transportation and military device, mainly because of their advantages such as high energy density, high power density, high charge-discharge efficiency and long cycling life (>100000 times). In the research and application of solar energy system, the combined form of supercapacitor and battery is used to replace the original combination of solar cell and battery, and the characteristics of supercapacitor with stable high-temperature performance and fast charging and discharging speed are fully utilized, which greatly improves the performance of energy storage system [1]. Not only that, in recent years, in the field of electric vehicles, supercapacitors have also made outstanding contributions. In order to solve the key problem of the non-monotonic energy consumption process accompanied by the change of frequency during the battery discharge process, research has shown a practical solution is to couple the battery with a supercapacitor as an energy storage system for electric vehicles, due to its higher rate capability and better cyclability [2]. Until now, supercapacitors have discovered the endless potential in the energy field. In the future, more scientists will invest in research and applications of supercapacitors, they will be used in various fields and bring outstanding contributions to human society.

In general, supercapacitors are composed of electrodes, current collectors, electrolytes and separator membrane [6], the stacked configuration as depicted in figure 1.1.

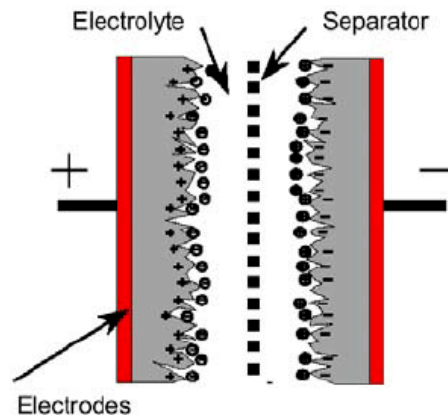


Figure 1.1 Structure of supercapacitor [46]

The function of the separator membrane is the same as that of the separator membrane in batteries. It separates the two electrodes, prevents short circuits between the electrodes, and allows ions to pass freely.

According to different energy storage mechanisms, supercapacitors can be divided into 1) double electric layer supercapacitors (EDLC), it uses the electric double layer interface between the electrode and the electrolyte to accumulate electric charge to store energy, during the charging and discharging process, electrons only enter and exit on the surface of the electrode through the external circuit. The cations and anions in the electrolyte move in the solution. There is no chemical reaction on the electrode, that is, no Faradic process is involved. Therefore, EDLC is highly reversible; 2) Faradic pseudo capacitors which derive capacitance from the storage of charge in redox materials in response to a redox reaction; 3) hybrid supercapacitors that mix the two mechanisms [7].

In addition, according to the structure of the supercapacitor, it can be divided into the symmetrical supercapacitor and asymmetric supercapacitor. If the material, shape, energy storage mechanism, etc. of the two electrodes of the supercapacitor are the same, it is called a symmetrical supercapacitor; if they are different, it is called an

asymmetrical supercapacitor.

1.2 Micro supercapacitors

The rapid development of portable electronic devices has greatly stimulated the strong demand for multifunctional and miniaturized electrochemical energy storage devices in modern society [8][9][10]. Among them, micro supercapacitors are new type of high-performance miniature electrochemical energy storage devices, its energy storage mechanism is the same as that of traditional supercapacitors [11]. Compared with miniature batteries, micro supercapacitors have the advantages of high-power density, fast charge and discharge speed, long lifetime and many others [12][13]. For now micro-supercapacitor is a kind of stand-alone power source which has a complement or even replacement for micro batteries [14]. Due to the advantages in electrochemical performance, they have received extensive attention from researchers, especially in the field of inconvenient disassembly devices such as microelectronic chips, biosensors, and implantable biomedical equipment [15].

Nowadays, the demand for flexible stretchable electronic devices continues to grow [16][17]. They can be stretched, bent, and folded without affecting performance and can be covered on any irregular surface such as human skin to achieve unprecedented novel applications. Therefore, in the future wearable and implantable electronic devices have broad application prospects. Flexible and stretchable electronics, such as electronic skin, nano-robots, embedded micro-medical devices, sensors. They have the characteristics of high integration, multi-function, good comfort, and reliable safety. This means that the corresponding energy supply unit also needs to make corresponding changes to cope with the new requirements put forward in the development of flexible and stretchable electronics. Micro supercapacitors have become one of the excellent choices for energy storage devices due to their small size, variable structure, high safety, and high comfort experience. In addition, the diversity and feasibility of micro-

supercapacitors in the selection of structures, electrode materials [18][19][20], electrolytes, various substrates and fabrication methods designed to improve the performance of micro supercapacitors and further broken the bottleneck of single-function flexible electronic devices, and the formed new processes are better integrated into more advanced and more flexible equipment.

1.2.1 Application of micro supercapacitors

For example: in 2016, Junyeong Yun et al. [21] developed a stretchable multifunctional integrated self-driving sensor system with a wireless charging device. The sensing system consists of a micro supercapacitor array, a NO₂ gas sensor, a photodetector, a pressure sensor and a wireless charging unit. It can be worn on the human body to realize independent monitoring of light, gas, pulse, sound and pressure, and meet people's needs. The basic requirements of wearable integrated electronics are expected to be put into the market to give full play to their practical application value.

In August 2021, an international team led by the famous German physicist Professor Oliver Schmidt has successfully developed the smallest bio-supercapacitor to date [22]. This energy storage system opens up possibilities for the operation of next-generation biomedical intravascular implants and micro-robot systems in small spaces of the human body. Besides, this energy storage device has a volume of only 0.001 cubic millimeters, which is 1/3000 of the previous smallest energy storage device. But it can still provide up to 1.6V power supply voltage for microelectronic sensors in the blood. The results of this research show that the micro supercapacitor has achieved a breakthrough in the medical field, and this technology will also have a wider range of applications in the future.

1.3 Graphene

Graphene is a two-dimensional planar structure formed by the periodic interconnection of carbon atoms through six-membered rings that can be expanded indefinitely, as depicted in figure 1.2 [48].

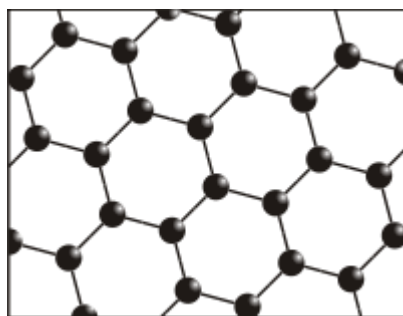


Figure 1.2 Graphene structure formed by carbon atoms

In 2004, physicists Andre Heim and Konstantin Novoselov at the University of Manchester isolated and investigated the material and were awarded the Nobel Prize in Physics in 2010 for their "groundbreaking experiments regarding the two-dimensional material graphene" [22]. Graphene is the world's thinnest material – it is only one atom thick, one million times thinner than a human hair. However, it is very strong, stronger than steel and diamond [23]. Graphene's unique atomic arrangement gives it many unique properties, excellent electronic conductivity (electron mobility can reach $200000\text{cm}^2/\text{Vs}$ [24]) and thermal conductivity (thermal conductivity can reach about 5300 W/mg [25]), large specific surface area (theoretical value can reach $2630\text{ m}^2/\text{g}$ [26]), high mechanical strength (breaking strength reaches 125 GPa [27]).

There are many ways to prepare graphene, micromechanical separation method, cut graphene flakes directly from larger crystals; SiC epitaxial growth method, which is to remove silicon by heating single crystal silicon carbide, and decompose graphene sheets on the single crystal surface; redox method, chemical vapor deposition method (CVD) so on and so forth [28][29][30][31][32][33].

Due to the unique two-dimensional structure of graphene (huge specific surface area), excellent electrical conductivity, good thermal conductivity, high stability, low noise, and special chemical and optical properties, these findings immediately attracted the interest of researchers in various fields, and continued investment and research. For example, research shows that the huge surface area makes graphene very sensitive to the surrounding environment and can be used to detect the release of gases or molecules [34]. At room temperature, graphene has high carrier mobility 10 times that of commercial silicon wafers, which is the most prominent advantage of graphene as a nanoelectronics device, so used to prepare graphene transistors [35]. Good light transmission and electrical conductivity, so that graphene has an outstanding application prospect in transparent conductive electrodes, which can be used for dye-sensitized solar cells [36]. Moreover, graphene and graphene oxide can be used in solar cells, seawater desalination, medical anti-cancer, biological antibacterial, supercapacitors, and many others [37][38][39][40].

1.3.1 Application of graphene in supercapacitors

The discovery of graphene immediately attracted significant attention from researchers in the field of supercapacitors because graphene possesses a very high theoretical specific surface area, excellent mechanical properties and electronic conductivity. From the perspective of supercapacitors, the electrode material is one of the main factors that determine its performance and the properties of graphene meet the needs of supercapacitor electrodes.

It is generally believed that the specific surface area will affect the size of the capacity, and the specific surface area is directly proportional to the electric capacity. The most mature electrode material for supercapacitors is activated carbon. The production cost of activated carbon is low and the process is simple. However, graphene has a higher specific surface area than activated carbon. In addition, activated carbon is

carbonized from coconut shells, apricot shells, petroleum coke so on and so forth, and may contain metal impurities. Redox reactions may occur in the electrolyte to affect the performance of supercapacitors. The difference between activated carbon and graphene is that graphene has an sp^2 structure, the chemical performance is more stable, and the production methods are diversified, which can ensure high purity without sacrificing the specific surface area. Therefore, in recent years, graphene has become a popular player in the production of supercapacitor electrodes.

Although graphene has the problem of low material packing density at the beginning, after in-depth research and exploration, the shortcomings of graphene are no longer 'threatening'. From graphene boosting activated carbon to graphene partially replacing activated carbon and then finally graphene completely replaced activated carbon. As a consequence, the excellent performance of graphene completely conquered researchers in the field of supercapacitors.

1.3.2 Laser-induced graphene supercapacitors

In recent years, porous graphene nanomaterials have attracted widespread attention from many scholars, especially in the field of supercapacitors, due to their excellent chemical and physical properties. Not only that, porous graphene as an electrode material for supercapacitors, on the one hand, is due to its porous characteristics, which is conducive to the full contact between the electrode material and the electrolyte and the transmission of electrolyte ions, and it has a large specific capacitance. On the other hand, porous graphene can be prepared with other conductive polymers and metal oxides into different three-dimensional graphene composite materials, comprehensively mentioning the electrochemical characteristics of electrode materials. As an environmentally friendly energy storage device, supercapacitors have the advantages of high power density and low pollution. To further expand the application range of supercapacitors, porous graphene nanomaterials, as a new type of electrode

material, in addition to using their own advantages of high specific area to improve the performance of electrochemical energy storage, but also through different preparation methods to achieve low pollution requirements.

As mentioned earlier, there are many ways to prepare graphene, among them, CVD is the main method for the early preparation of three-dimensional porous graphene. However, this method is not accurate enough to control the morphology of the final graphene, and the shortcomings of this method still exist: the preparation process requires high-temperature conditions, and the production process is costly and cumbersome.

As a result, new technologies have emerged as the requirements for the environment and costs have increased. The conversion process of polymeric substrate into graphitic materials was already known in the 60s. In 2014, Lin et al. [41] used a method of directly writing graphene pattern structures on commercial polyimide (PI) films using CO₂ infrared lasers under ambient conditions, as depicted in figure 1.3, produced "laser-induced graphene (LIG)" for the first time. The energy generated by the laser will vibrate the lattice of the irradiated area, which makes the local temperature extremely high. This high temperature can easily destroy the C—O, C=O, and N—C chemical bonds. Subsequently, the carbon atoms will be rearranged to form a graphene structure, and the remaining atoms will recombine and be released in the form of gas. The sp³-carbon atoms are photothermally converted to sp²-carbon atoms by pulsed laser irradiation. For ultraviolet lasers, the conversion of LIG is mainly a photochemical reaction, because ultraviolet light has a short wavelength and high energy, which can directly break chemical bonds [42]. For visible light lasers, photothermal effects and photochemical reactions may exist at the same time. It is worth noting that the successful preparation of laser-induced graphene has nothing to do with the type of laser and the working wavelength, but with the output power, exposure time and

thermal effect. Therefore, as long as the power density of continuous and pulse laser past a certain threshold can complete LIG, there is no doubt that this will bring convenience to production.

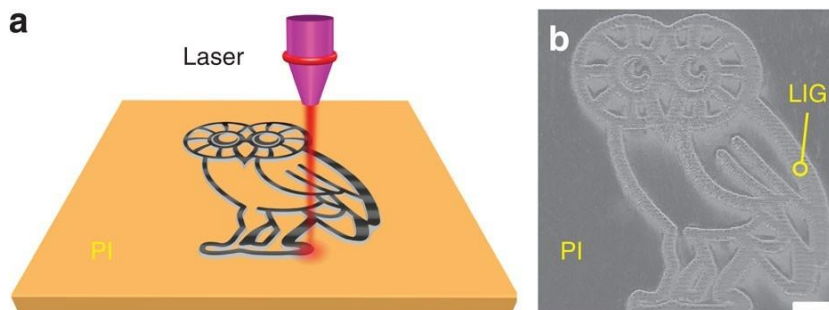


Figure 1.3 LIG products on PI (a) Processing schematic diagram of laser-induced graphene prepared by using a CO₂ laser to ablate PI; (b) Scanning electron microscopy image of LIG, the pattern is owl-shaped, and the scale bar is 1 mm [42].

Under the control of computer software, LIG is a convenient, operable, and high-precision technique. The pattern can be successfully transformed into a designed shape through the set laser parameters. In conclusion, LIG technique shows its unique advantages of the simple preparation process, low cost, high efficiency and environmental protection compared with the others graphene-fabrication techniques. Nowadays, LIG has become an effective method in the fabrication and integration of supercapacitors.

1.4 The effect of electrode impedance on supercapacitors

We have learned that the basic structure of a supercapacitor is composed of electrolyte, electrodes, current collectors and separators. To improve the electrochemical performance of supercapacitors: capacitance, power density, and energy density, more and more scholars are studying the constituent materials for the structure of supercapacitors. Among them, electrolytes and electrodes are the most important factors affecting the performance of supercapacitors. Therefore, this chapter

starts with the regulation of electrode materials and the comparison of electrolytes to improve the energy storage efficiency of supercapacitors.

To optimize the use of supercapacitors, it can be done by reasonably controlling the components of the supercapacitor. Therefore, the establishment of a model that can accurately reflect the actual working characteristics of supercapacitors has important research significance for the rational use of supercapacitors, performance optimization and system simulation. Among them, the equivalent circuit is the most practically used model. It uses basic circuit elements (resistance, capacitance, and inductance) to simulate the working characteristics of supercapacitors, as shown in figure 1.4. This method is simple and intuitive, which is convenient for analysis, calculation and model simulation.

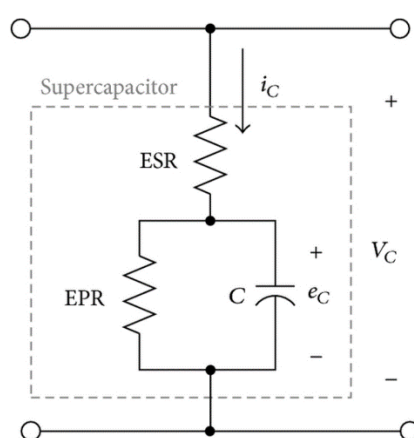


Figure 1.4 The equivalent circuit of supercapacitor [59]

ESR (equivalent series resistance) is one of the key performance indicators of supercapacitors. The specific meaning is the series connection of various small capacitances and resistances of supercapacitors, and by observing the equivalent circuit model of supercapacitors, it can be known that electrode resistance, electrolyte resistance and contact resistance constitute internal resistance, which directly affects the ESR.

The effect of ESR on supercapacitors is: the increase of ESR will reduce its ability to store charge, so the capacitance will decrease; ESR indirectly represents the power consumed by the internal heating of the capacitor, which has a greater impact on the charging and discharging process of the supercapacitor; The higher the ESR value, the lower energy efficiency.

Consequently, for laser-induced porous graphene supercapacitors, to improve its energy storage performance, reducing its electrode resistance is the primary task.

1.5 Electrolytes

The electrolyte is an important part of supercapacitors, it is mainly composed of electrolyte salt and solvent, which provides ionic conductivity and promotes the charge compensation of the electrode. The conductivity and electron mobility of the electrolyte performs a serious role in the internal resistance of supercapacitors, thereby affecting the energy storage capacity of supercapacitors. The properties of the electrolyte include ion type and size, ion concentration and solvent, the interaction between ions and solvent, interaction between electrolyte and electrode material, electrochemical window, and many others.

Energy density is one of the performance indicators of supercapacitors, increasing the working voltage can increase the energy density more effectively, and the working voltage strongly depends on the electrochemical window of the electrolyte. Ideal electrolyte requires a wide electrochemical window, high ionic conductivity, high electrochemical stability, wide operating temperature range, low volatility and flammability, environmentally friendly, low cost. Based on the research and report from literature, the electrolytes are classified into several categories as shown in figure 1.6 [50], including aqueous, organic, ionic liquids, solid-state or quasi-solid-state, as well as redox-active electrolytes.

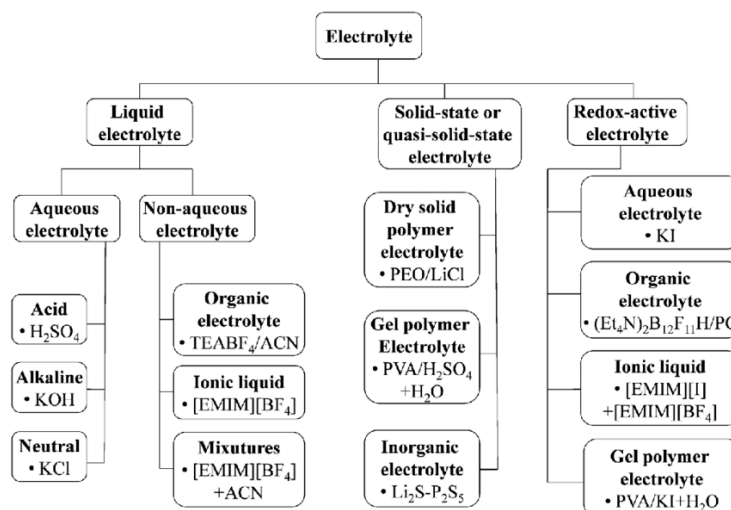


Figure 1.5 Classification of electrolytes for electrochemical supercapacitors

The type of electrolyte is selected according to the characteristic of the electrode material, rarely, electrolytes can fully fit the electrodes because different electrolytes have their advantages and disadvantages.

1.5.1 Aqueous electrolyte

Compared with organic electrolytes and ionic electrolytes, aqueous electrolytes have higher ionic conductivity [51]. In addition, they are widely used due to their low price and easy preparation. But because the voltage window of water is only 1.23V, therefore, the working voltage of the aqueous electrolyte is relatively low. Additionally, the main body of the aqueous electrolyte is water, so it will be affected by temperature, and the operating temperature is required to be controlled below the boiling point of water and above the freezing point.

Aqueous electrolytes can be divided into acidic, alkaline, and neutral electrolytes.

(1) Acid electrolyte

The representative of acidic electrolyte is H_2SO_4 aqueous solution, however, considering that the H_2SO_4 aqueous solution is a strong acid, it is corrosive to some equipment, which makes it impossible for supercapacitors to use metal as the current collector. The advantage is the high conductivity, for example, at $25^\circ C$, the ionic

conductivity of 1mol/L H₂SO₄ solution is 0.8S cm⁻¹ [51].

(2) Alkaline electrolyte

Alkaline electrolyte usually uses strong bases such as KOH and NaOH as electrolytes. On one hand, unlike strong acid electrolytes, alkaline electrolytes will not be so corrosive, so supercapacitors can use metal as the current collector. On the other hand, the conductivity of the alkaline electrolyte is lower than that of acid electrolyte, for example, the conductivity of 25°C, 6mol/L KOH is the largest, which is 0.6S cm⁻¹ [51]. It is worth noting that the concentration of alkaline electrolytes may cause hydrogen evolution reactions and affect the specific capacitance of supercapacitors [52].

(3) Neutral electrolyte

Neutral aqueous solutions have a wider working window than acidic and alkaline solutions, typical neutral solutions are potassium salt, ammonium salt, lithium salt and sodium salt. Among them, Na₂SO₄ is the most commonly used neutral electrolyte. Demarconnay et al. [53][54] applied Na₂SO₄ electrolyte to the preparation of activated carbon symmetrical supercapacitors for the first time, increasing the working voltage of aqueous water-based supercapacitors from 1V to 1.6V.

1.5.2 Organic electrolyte

Organic electrolytes have a higher electrochemical window (2.5V~2.8V), so the commercial market relies more on organic electrolytes. However, compared with water-based electrolytes, organic electrolytes have insurmountable disadvantages such as high cost, toxic, flammable and explosive. In addition, organic electrolytes have stricter requirements for purification and packaging and try to avoid contamination by impurities. When choosing a suitable organic electrolyte, in addition to considering the conductivity, the ion size of the organic electrolyte and the adaptation of the carbon material pore size should also be considered, to improve the adaptability to increase the specific capacitance of the supercapacitor. The organic electrolyte is mainly composed of solvent and electrolyte salt. The most commonly used organic solvents are propylene

carbonate (PC) and acetonitrile (ACN), the main features are high dielectric constant, good stability and low volatility. Cationic electrolyte salts mainly include lithium salt series (Li^+) and quaternary ammonium salt series (R_4N^+), such as tetraethylammonium (Et_4N^+), triethylmethylammonium (Et_3MeN^+), trimethylethylammonium (Me_3EtN^+); Commonly used anion organic electrolyte salts include lithium tetrafluoroborate (LiBF_4), lithium hexafluorophosphate (LiPF_6), tetraethylammonium tetrafluoroborate (TEABF_4), triethylammonium tetrafluoroborate (TEMABF_4).

1.5.3 Ionic liquid electrolyte

A substance composed of positive and negative ions that is liquid at or near room temperature is called room-temperature ionic liquid (IL), also called room temperature molten salt. Ionic liquid has characteristics such as wide electrochemical window, high thermal stability, high chemical stability, low toxicity, non-flammability and negligible volatility. Therefore, the application of ionic liquid electrolytes in SCs has received great attention. The most commonly used ionic liquid electrolyte cations include pyrazole cations, pyrrole cations, imidazole cations, quaternary ammonium cations, and many others [55]. For example, the potential window of imidazolyl EDLCs can reach 3.0V~3.2V [55], while that of pyrrolyl can reach 3.5V~3.7V [56]. The anions are mainly composed of BF_4^- , PF_6^- and bis(trifluoromethylsulfonyl)imide (TFSI-) [55].

Compared with aqueous electrolyte, the disadvantage of ionic liquid electrolyte is its lower conductivity (usually less than 10mS cm^{-1}), but due to the high selectivity of anion and cation in ionic liquids, the combination of anion and cation is optimized to improve physical and chemical properties, such as electrochemical window, conductivity, and many others. Give an example, N,N-Diethyl-N-methyl-N-(2-methoxyethyl)ammonium tetrafluoroborate (DEME- BF_4) have been evaluated it has a wide potential window (6.0V) and high ionic conductivity (4.8 mS cm^{-1} at $25\text{ }^\circ\text{C}$) [57]. In terms of high-temperature applications, the electrochemical performance of 1-ethyl-

3-methylimidazole bistrifluoromethanesulfonimide salt ([EMIM][TFSI]) ionic liquid electrolyte remains the best when the temperature is higher than 80°C, it has the potential to become a high-temperature electrolyte for high-performance supercapacitors [57].

Chapter 2 Laser parameters

2.1 Van der Pauw method

The Van der Pauw method, also known as the four-point measurement method, is a method of measuring the sheet resistance of a sample [44]. This four-wire method is used on small flat samples with four terminals and uniform thickness. The current is applied to the sample through two terminals, the voltage is measured through the opposite two terminals, and then the resistivity is calculated from the voltage and the set constant current value.

The system of laser machine is controlled by computer, various of geometries could be designed according to our demands. Herrin, in order to cooperate with the Van der Pauw method to measure the resistance of porous graphene, a sample cross with the four corners protruding and the middle solid was designed on the computer, as depicted in figure 2.1, the four corners are square structure, the width is 1.4 mm, and the connection length of the square protrusion is 1 mm.

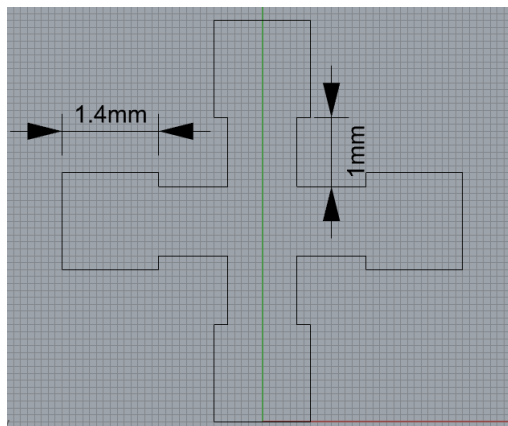


Figure 2.1 The design of Van der Pauw cross

2.2 Laser parameters effects the impedance of graphene

Laser conversion of polymers has been studied since the early 1980s [43], for the last 20 years, more and more papers describing this phenomenon and the application of laser ablation becomes mature. Many papers give evidence that the lasing parameters have a profound effect in controlling the chemical and physical properties of LIG. Herein we further study laser parameters and focus on the physical properties of LIG in order to minimize the sheet resistance.

As mentioned earlier, the formation of LIG is not affected by the type of laser and laser machine, and the final formation and quality of LIG are determined by the output energy of the laser. Therefore, in order to find the graphene with the smallest sheet resistance, evaluate the electrical properties of graphene by applying different laser parameters.

A flexible PI film (Kapton) with a thickness of 125 μ m which was used as the substrate for carbonization, the pattern transformed on PI is the designed Van der Pauw cross, the LIG are fabricated using a micromachining system produced from CHILAB, equipped with a CO₂ pulsed laser working at 1064nm wavelength, with tunable process parameters (velocity, frequency, power, raster, and many others).

Varying the frequency from 5kHz to 20kHz in 5kHz increments, the velocity from 300mm/s to 450mm/s in 25mm/s intervals, the raster from 100dpi to 1000dpi in 100dpi intervals, and the power is set between 10% and 19%. During the experiment, five LIG cross samples were printed for each set of laser parameters, five samples as a group, as shown in figure 2.2, the appearance of the LIG samples formed under each laser parameter are different, thus the quality of the samples varies from good to bad. Some samples broken down with large black shadow and PI bend badly as shown in figure

2.2(d) and as figure 2.2(b) shown some crosses, its width becomes larger. What's more, some crosses are not fully carbonized, part is converted into graphene and part is still PI substrate or even have no carbonization traces at all, as shown in figure 2.2(c). The shape of the LIG that best meets our expectations is figure 2.2(a), the outline of the pattern edge is clear, without damage the shape of crosses, and the substrate is not bent.

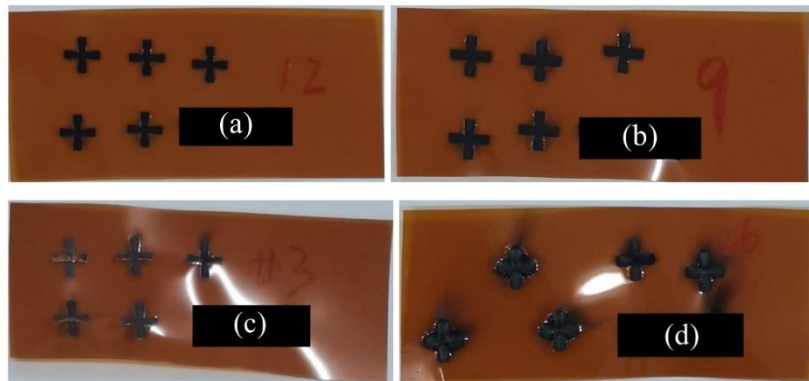


Figure 2.2 LIG Van der Pauw crosses

The principle of LIG is that the energy of the laser output generates high temperature in a short time to break the chemical bond of the substrate material and recombine it. But what is not neglected is the thermal expansion, thermal diffusion and thermal stress during the preparation process. These thermal effects will cause the bending of the PI substrate and have a serious impact on the shape and quality of the LIG.

Before using the Van der Pauw method to measure the sample, in order to reduce the error caused by the poor conductivity of the measuring instrument and the sample, the four protruding corners of the sample were covered with a thin layer of silver paste, as shown in figure 2.3, with the aim of improving the conductivity and the accuracy of measurement result.

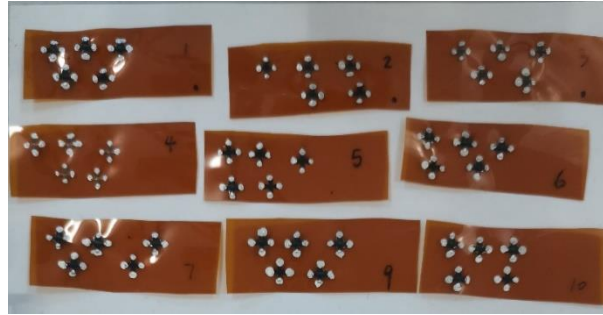


Figure 2.3 Van der Pauw crosses covered with silver paste

Measure the voltage of each sample under the constant current 0.1 mA, calculate the resistance value by Ohm's law, the laser parameters tested in this work are summarized in table 2.1, where the samples are named by different laser parameters, and “none” in the reported table means not proper graphitization. There are five samples under each group of laser parameters, corresponding to five resistances. In order to draw more accurate conclusions, find the average resistance (R) and variance resistance (σ) of each group.

Sample Name	Raster [dpi]	Power [%]	Frequency [kHz]	Velocity [mm/s]	R1 [Ω]	R2 [Ω]	R3 [Ω]	R4 [Ω]	R5 [Ω]	R [Ω]	σ [Ω]	
Frequency Sweep												
1	600	10	5	375	2.35	1.52	none	1.65	1.20	1.68	0.49	
2	600	10	10	375	2.65	1.83	4.00	3.76	4.15	3.28	1.00	
3	600	10	15	375	none	4.00	7.46	none	4.60	5.35	1.85	
4	600	10	20	375	none	none	none	none	none	none	none	
Velocity Sweep												
5	600	10	5	300	1.34	2.50	1.48	4.48	2.02	2.36	1.27	
6	600	10	5	325	1.50	1.10	9.56	2.04	none	3.55	4.03	
7	600	10	5	350	1.80	2.12	1.97	2.03	4.67	2.52	1.21	
8	600	10	5	375	2.34	none	1.98	2.11	2.34	2.19	0.18	
9	600	10	5	400	2.42	1.43	2.15	2.32	2.65	2.19	0.46	
10	600	10	5	425	2.90	1.22	1.98	2.03	3.61	2.35	0.92	
11	600	10	5	450	2.80	1.92	1.98	2.60	2.90	2.44	0.46	
12	400	19	5	300	10.93	3.94	3.57	4.90	4.33	5.53	3.06	
13	400	19	5	325	3.70	3.45	3.70	4.06	3.57	3.70	0.23	
14	400	19	5	350	4.08	3.70	3.35	3.70	4.05	3.78	0.30	
15	400	19	5	375	3.68	3.95	3.64	3.50	4.15	3.78	0.26	
16	400	19	5	400	2.97	4.72	3.16	2.82	2.92	3.32	0.79	
17	400	19	5	425	3.70	2.84	3.85	2.60	2.51	3.10	0.63	
18	400	19	5	450	3.85	3.20	3.42	3.26	2.76	3.30	0.39	
DPI Sweep												
19	100	10	4	125	none	none	none	none	none	none	none	
20	200	10	4	125	none	none	none	none	none	none	none	
21	300	10	4	125	15.86	11.10	11.16	17.07	12.34	13.51	2.78	
22	400	10	4	125	4.63	4.80	3.28	3.22	2.25	3.64	1.07	
23	500	10	4	125	2.80	2.51	none	1.68	3.60	2.65	0.79	
24	600	10	4	125	2.88	none	1.05	none	1.23	1.72	1.01	
25	700	10	4	125	42.30	1.02	27.30	none	1.27	17.97	20.37	
26	800	10	4	125	1.08	1.00	1.58	1.76	0.94	1.27	0.37	
27	900	10	4	125	0.04	2.58	none	1.42	0.38	1.11	1.15	
28	1000	10	4	125	2.90	8.40	0.40	none	0.13	2.96	3.84	
29	100	10	4	200	none	none	none	none	none	none	none	
30	200	10	4	200	none	none	none	none	none	none	none	
31	300	10	4	200	9.22	12.22	8.47	13.32	none	10.81	2.33	
32	400	10	4	200	1.10	1.50	none	none	none	1.30	0.28	
33	500	10	4	200	1.40	2.30	2.90	none	3.34	2.49	0.84	
34	600	10	4	200	0.25	0.40	none	none	none	0.33	0.11	
35	700	10	4	200	0.73	0.56	1.36	0.63	0.74	0.80	0.32	
36	800	10	4	200	0.04	none	6.67	none	none	3.36	4.69	
37	900	10	4	200	1.82	3.33	0.57	5.00	none	2.68	1.91	
38	1000	10	4	200	1.45	1.18	4.27	1.10	none	2.00	1.52	

Table 2.1 Experimental laser parameters

By observing table 2.1, some fascinating facts could be found: when the raster is only 100dpi and 200dpi, no matter how high the speed, the PI cannot absorb enough energy to be converted into LIG when the power is constant, like samples 19, 20, 29, 30; focusing on the speed, starting from sample 19, there are many sets of samples that are incomplete, because carbonization was not complete, so the resistance was not measurable. When the speed is 125mm/s and 200mm/s, the average resistances become unstable and the variance are large, which are not ideal results; By looking at samples 1, 2, 3, 4, when the frequency is increasing, and the average and variance of the resistance is also increasing, even when the frequency reaches up to 20kHz, there is no trace of carbonization on the PI. From the parameters of the other groups, keeping the frequency at 4kHz and 5kHz is beneficial to the formation of LIG.

From table 2.1, we can only roughly see the influence of each laser parameter on the LIG resistance, so in order to find out the relationship between the various parameters more vividly, the 3D diagram can be used. As figure 2.4 shows, the color bar on the right of the figure indicates that red means the highest resistance value, while purple means the lowest resistance value, each color area has a corresponding resistance value. figure 2.4(b). studies the effect of speed and frequency on the resistance of samples, speed and frequency are on the abscissa and resistance is on the ordinate. Decreasing frequency and speed at the same time, we find that the color in the 3D diagram gradually approaches purple, which means that the resistance is getting smaller and smaller. Observing in the direction of increasing speed, the color changes from purple to yellow and finally to red, indicating that the resistance is gradually increasing. The conclusion is that frequency and speed are positively correlated. Therefore, to minimize sheet resistance of LIG, frequency and speed must be reduced.

The relationship between raster and speed effects resistance is investigated in figure 2.4(a). The greater the raster, the color turns into purple gradually, which means the

smaller resistance at the same time the speed is also decreasing. Hence, it can be judged that the speed and raster are negatively correlated to influence resistance.

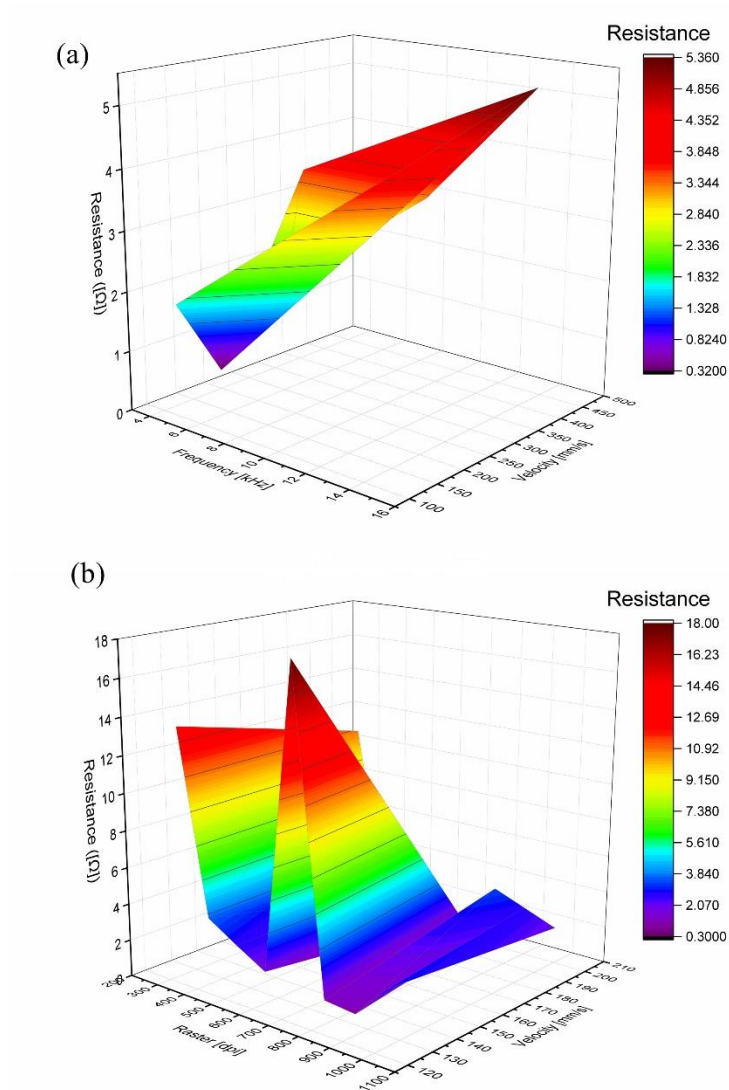


Figure 2.4 The change of resistance with different laser parameters (a) resistance with respect to the change of raster and velocity (b) the resistance as a function of the change of frequency and velocity.

In summary, from these two figures, it can be seen that the influence of speed on the resistance is the same, reducing the speed would help minimize resistance, also increasing raster and decreasing frequency is meaningful. In addition, considering the resistance variance, which is the stability of LIG quality, so considering the resistance

value and variance so we choose a suitable laser parameter range for LIG preparation:
keep power is 19%, raster is 400dpi and frequency is 5kHz, like samples 15~18.

Chapter 3 The device design

3.1 three-electrode system

Two-electrode system, that is, the anode and the cathode are called as the working electrode and the reference electrode. There is only one electrical circuit when the two-electrode system works, the anode is the electrode surface where the oxidation reaction occurs while the cathode is the electrode surface where the reduction reaction occurs.

As can be seen in figure 3.1 [58], the three-electrode system has three electrodes, namely the reference electrode, the working electrode and the counter electrode. The three electrodes can be close but not connected. The three-electrode system contains two circuits. One circuit is composed of a working electrode and a reference electrode to test the electrochemical reaction process of the working electrode, and the other circuit is composed of a working electrode and a counter electrode to form a circuit where current can flow.

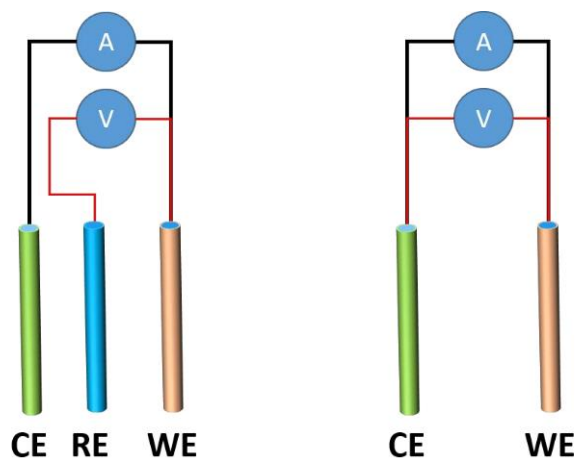


Figure 3.1 The difference between three-electrode and two-electrode systems

In the electrochemical test, a single electrode is studied. In a two-electrode system, the counter electrode and the reference electrode are at the same potential. Due to the

large current passing through, the voltage drop of the solution and the polarization of the counter electrode are generated, in this way, the potential measured by the working electrode is not accurate. Therefore, the three-electrode system is the first choice to design our devices.

The selection criteria for the electrode are that the electrode does not react with the electrolyte, the surface is smooth, the property is stable, and the resistance is small.

In our experiment, use the metallic mask to print interdigitated LIG samples instead of designing geometry by computer to direct laser write for the reason that laser repeatability with geometry can be low under certain circumstances dependent upon laser parameters and geometries.

As shown in figure 3.2, the metallic mask has a narrow gap in the middle, which has two individuated parts. According to the experimental design of interdigitated electrode pattern, one side is 6 digits while the other side is 5 digits. Based on the previous research on laser parameters, it has been found out a range of parameters to minimize sheet resistance of graphene-based electrodes. The printing method is to put the cleaned mask on the PI, use tape to keep the mask in contact with the PI substrate to reduce the gap between them, and then select a laser scanning area, which is larger than the mask, and the printed samples are as shown in figure 3.2.

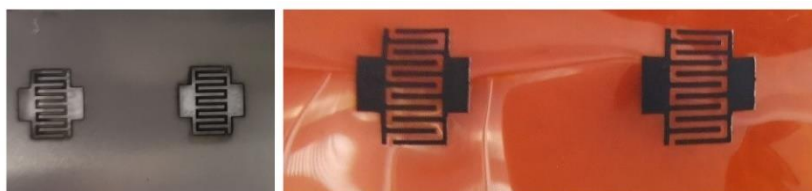


Figure 3.2 The original mask and interdigitated LIG samples

3.2 Preparation and assembly

The preparation of supercapacitor materials is based on its structure and packaging: electrolyte ([EMIM][TFSI] and [PYR14][TFSI]), electrodes (LIG), separator (glass fiber separator), current collectors, glass substrate.

All the components (except pouch cell materials and sealing ones) used to assemble the device were dried by means of vacuum oven (Buchi) with a procedure of 1h heating at 60°C, 12h at 120°C and 1h at 60°C.

Prepare 5ml of distilled water, pour 50mg of sodium carboxymethyl cellulose (CMC, provided by MTI) into the distilled water, place it on the stirring hot plate, keep rotating until it is completely dissolved and keep the temperature at 60°C, the final state is gelatinous, then add 100mg carbon black (provided by Imerys) and 850mg YP-50F (provided by Kuraray) to the mixed gel in batches, stir continuously for 30 minutes until all the powder are completely dissolved, and the final product is black viscous gel. Next, cut a piece of aluminum foil of a suitable size (length is about 7cm, width is not limited), and evenly spread the prepared AC gel on the upper end of the aluminum foil, with a thickness of 200 μ m. Then the coating was left dry through convection and counter electrodes were cut of 7cm x 0.5cm.

Packaging is the last and extremely important step in assembling LIG supercapacitors. The purpose of this step is to prevent the pollution and other impurities and prevent the volatilization and overflow of electrolyte. In addition, it can prevent the intrusion of external moisture and protect the integrity of the entire SC structure. In this experiment, flexible package made of aluminum-plastic laminate film is used as the outer shell of the supercapacitor. The packaging material was cut in 5cm x 5 cm in order to avoid material over-consumption and to let the sealing process not to alter the cell or

damage it. For the packaging of the cell, the use of mature processes such as electroplating, etching, printing, laser, and hot pressing can greatly improve the reliability of the device. Among them, the hot-pressing process was easy, efficient, and fast, this was needed to allow the aluminum tab to be sealed to the polymer film on the pouch cell foil. The material required for the hot-pressing process is hot melt tape, the size of hot melt tape is 3cm in length and 1cm in width. Moreover, the plastic film melted on the aluminum tabs further decreases the conductivity between the electrodes.

Generally, the structure of a supercapacitor is a stacked layer, and the structure determines the assembly sequence. From bottom to top, a layer of non-conductive glass substrate is a material used to hold the LIG electrodes and is the first layer of the entire structure. Fix the sample on the glass with tape, contact current collectors to the working electrode and the reference electrode, as shown in figure 3.3, for the asymmetric sample, the contact areas are 0.5cm x 0.2cm in width on these two electrodes (6 digits is the working electrode and 5 digits on the other side is the reference electrode).



Figure 3.3 A LIG sample assembling

Next, place the separator upon the sample, cover the area of the interdigitated parts only. Then slowly drop 150 μ L IL electrolyte into the separator, place the aluminum thin strip with AC on the separator immersed in the IL electrolyte. Afterward, place another

piece of glass on the top layer to fix the entire structure. Until this step, the three-layer structure of the electrochemical cell is completed. During the assembly process, it is worth noting that there must be enough space between two current collectors to prevent contact and damage to the current loop. Therefore, it is necessary to fix their respective positions. Besides, try to avoid IL electrolyte dripping outside the separator or too much IL electrolyte because the amount of electrolyte as well as its localization within the electrochemical cell are important in order to let the measurement stable and each electrochemical cell could be comparable with the electrolyte condition fixed.

Then use the heat-sealing method to seal three sides of the pouch cell foil, the left side is to put the assembled cell into the pouch cell foil. For the left side, the three current collectors draw out, to prevent contact with each other and short-circuit, it is necessary to paste a layer of black insulating tape on the outer layer of the pouch cell foil before sealing. The inner side is glued together with hot-melt tape and insulating tape, and then the last side of the pouch cell foil is sealed in the same way. As a result, the inside of the pouch cell foil is in a vacuum state, which has the advantage of avoiding the influence of oxygen and other gases in the air in addition to moisture and other impurities. The reason is that oxygen can be dissolved in the electrolyte, and oxygen consume the charge stored in the supercapacitor in the form of reduction reaction, thereby affecting the performance of the supercapacitor. After ensuring the integrity of the packaging, a LIG supercapacitor is successfully prepared.

3.3 Main performance indicators of supercapacitors

The main electrical parameters of supercapacitors to be evaluated are cell capacitance (C), operating voltage (V), equivalent series resistance (R_{ESR}), power density (P), energy density (E), coulombic efficiency (CE) and cycle stability.

(1) Cell capacitance

In supercapacitors, each electrode is a capacitor. Therefore, for supercapacitors, the

total capacitance is derived from the series connection of the positive and negative capacitors. Generally, the specific capacitance of supercapacitors is divided into two types, one is mass specific capacitance: the capacitance value per unit mass; the other is volumetric specific capacitance: the capacitance value per unit volume. In fact, the weight of graphene is difficult to know and is small enough to be negligible, so we prefer the areal capacitance than mass capacitance.

The calculation formula of capacitance is as follows:

$$C = \frac{I \Delta t}{\Delta V} = \frac{Q_{dis}}{\Delta V} \quad (3.1)$$

C is capacitance which is proportional to the charge (Q) and inversely proportional to the operating voltage (ΔV).

(2) Operating voltage

The operating voltage also called voltage window, is the best working voltage for the supercapacitor. Electrolyte, operating temperature are key parameters to affect the operating voltage. If it is operated for a long time beyond this voltage value, the life of the supercapacitor will be shortened and may cause permanent damage, so it is not recommended to exceed the operating voltage to test supercapacitors.

(3) R_{ESR}

The equivalent series resistance of a supercapacitor refers to the series resistance between the positive electrode and the negative electrode, and it has a great relationship with the electrode material, electrolyte, and assembly method. Generally, ESR can be read in Nyquist plot.

(4) Power density and energy density

Energy density and power density are the two most important parameters to measure the performance of supercapacitors. The greater the energy density, the more electric energy the supercapacitor can store; the greater the power density, the more energy the supercapacitor can release per unit time.

The calculation formula of energy density is as follows:

$$E = \frac{CV^2}{2} \quad (3.2)$$

It can be seen from equation 3.2 that the energy density E (Wh cm^{-2}) is proportional to the square of the capacitance (mF) and the operating voltage. To increase the energy density of a supercapacitor, we must consider both the capacitance and the operating voltage.

The calculation formula of maximum power density is as follows:

$$P = \frac{V^2}{4R_{ESR}} \quad (3.3)$$

And the formula of power density during each cycle is calculated by:

$$P = \frac{E_{dis}}{t_{dis}} \quad (3.4)$$

It can be seen from equation 3.3 that the power density P (W cm^{-2}) is inversely proportional to the electrode equivalent series resistance R_{ESR} (Ω). Therefore, there are two ways to improve the maximum power density of supercapacitors, low-resistance electrode materials must be used and increase the operating voltage, but it is more effective to improve the power density by increasing the operating voltage according to equations 3.2, 3.4.

To compare the energy density of various devices, Ragone plot can be used to plot the energy density versus power density, as shown in the figure 3.4, both axes are logarithmic.

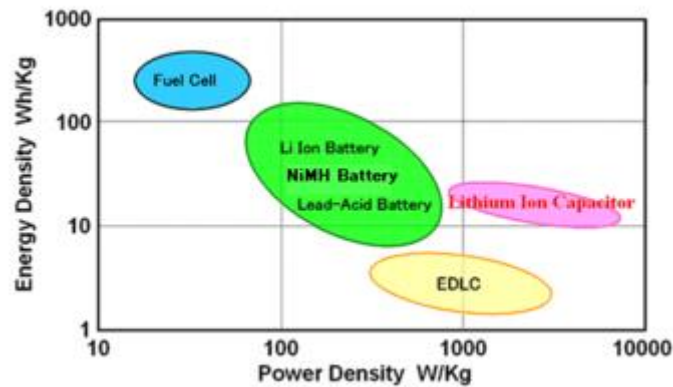


Figure 3.4 Ragone plot [62]

(5) Coulombic efficiency

Coulombic efficiency (CE), also called charging efficiency, refers to the ratio of the discharge capacities of the supercapacitor to the charging capacities during the same cycle. Because the input power is often not used to convert the active material into a charged state, but part of it is consumed (for example, the irreversible reaction occurs), so the coulombic efficiency is often less than 100%.

The calculation formula of CE is as follows:

$$CE = \frac{C_{dis}}{C_{ch}} \quad (3.5)$$

C_{ch} is charge capacities (mF) and C_{dis} is discharge capacities (mF).

(6) Cycle stability

Cycle stability refers to the ability of a supercapacitor to maintain electrical performance after multiple charges and discharges. It is mainly reflected in whether the attenuation of the capacitance value and energetic efficiency after multiple charge/discharge cycles is too large. For the reason that as the cycle continues, the activity of the active material to store charges decreases, and the performance of the supercapacitor declines, and the number of cycles corresponding to the sharp decline in performance is the life of the supercapacitor.

3.4 Electrochemical performance evaluation techniques

There are three main methods for measuring the performance of supercapacitors: open circuit voltage (OCV), cyclic voltammetry (CV), electrochemical impedance spectroscopy (EIS), galvanostatic charge and discharge (GCD) and float test.

The following introduces the specific parameter settings of the supercapacitor performance evaluation techniques based on the VPM3 workstation. For a fair comparison, all the measurements have been run according to the following experiments and the consistent settings.

(1) Open circuit voltage

The open circuit voltage measured here refers to the potential difference between the positive and negative electrodes of the supercapacitor when no current flows. In the our three-electrode system, the potential established by the two electrodes (the working electrode and the reference electrode) is mostly stable, so the open circuit voltage is the difference between the stable potentials of the two electrodes. Put the OCV test first because if the open circuit voltage is stable and not too high (with fluctuations within a certain range, generally $-1V\sim 1V$), it proves that the cell is “normal” and the system is stable.

(2) CV or voltammogram

CV is an electrochemical testing technique in which voltage is controlled and current is measured. For supercapacitors, the CV test is done at a certain scan rate. In the charging state, the current is positive, while the discharge is negative. Observe the current change within the specified scanning voltage window. Figure 3.5 shows the CVs at different scan rates (with different colors), increase the scan rate, the capacitance of the supercapacitor increases, which can be known by the equation 3.1.

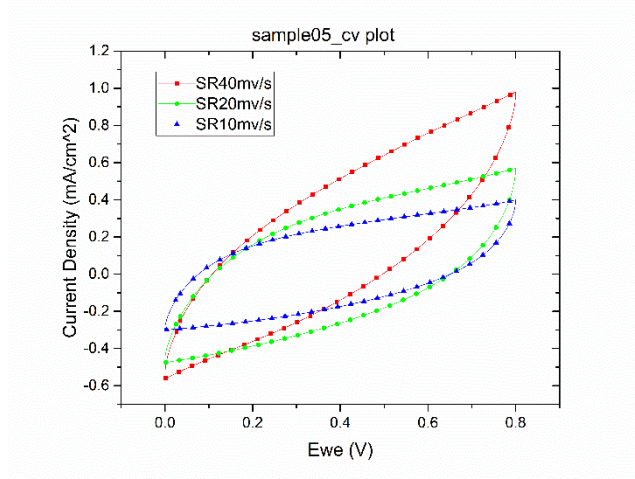


Figure 3.5 CVs at multiple scan rates

The electrochemical cell for the anodic and cathodic exploits the supercapacitor configuration but one electrode is the working and the other is the reference, then we add a counter for the three-electrode measurement setup and/or for the device measurement but in this case, we switch the reference and counter so that the two LIG electrodes are the ones constituting the device.

Anodic and cathodic measurements are exploited to evaluate the electrochemical performance of the material with respect to the electrolyte in such polarization conditions. We use these measurements to design the device.

Whether it is an anodic test or a cathodic test, the scan rate is constant at 5mV/s

- Anodic test

the voltage range of the first group is 0V~0.2V, the high potential of the forward scan is 0.2V (relative to V_{oc} : open circuit potential), and the low potential is 0V, oxidation current (I_{ox}) is generated during the whole process, and the obtained current-potential curve is called anodic polarization curve; In the reverse scan, the high and low potentials are reversed, the whole process produces a reduction current (I_{red}), and the obtained current-potential curve is called the cathodic polarization curve. Two

polarization curves form a cyclic voltammetry curve. For each sequence, change the high potential of the forward scan from 0.2V to 2V with an increment of 0.1V, that is, there are 19 steps, cycle 20 times per step, which means the charge/discharge cycle number is 380 for one anodic test.

- Cathodic test

The scan voltage range is -0.2V ~0V for the first sequence, the high potential of the forward scan is -0.2V (relative to V_{oc}), and the low potential is 0V. The potential range of each sequence is increased in 0.1V intervals until the last sequence is -3.5V ~0V, the number of cycles for each sequence is the same as the anodic test is 20 so the total number of charge/discharge cycles for one cathodic test is 560.

In the capacitance performance test, during the first scan, the initial CV cycle may be only the activation process of the electrode material, the CV curve could not be completely closed and cannot be used to calculate the specific capacitance. Thus, it is necessary that cycling several times to select the best cycle. In this experiment, each sequence loops 20 times, and the last loop generally is the most stable and effective, so in the subsequent calculation and analysis, only the last set of loop data are selected to calculate the specific capacitance.

Selected parameters like time, voltage, and currents to be analyzed from the CV diagram were export to MATLAB to calculate the charge quantity (Q_{ch}), discharge quantity (Q_{dis}), charge energy (E_{ch}), discharge energy (E_{dis}), coulombic efficiency (η_C) and energetic efficiency (η_E), and then use the following formula to calculate the areal capacitance of discharge ($C_{dis,S}$).

$$Q_{ch} = \int I_{ox}(t)dt \quad (3.6)$$

$$Q_{dis} = \int I_{red}(t)dt \quad (3.7)$$

$$E_{ch} = \frac{1}{2} \cdot Q_{ch}^2 \cdot V_{app} \quad (3.8)$$

$$E_{dis} = \frac{1}{2} \cdot Q_{dis}^2 \cdot V_{app} \quad (3.9)$$

$$\eta_c = \frac{Q_{dis}}{Q_{ch}} \quad (3.10)$$

$$C_{dis,S} = \left(\frac{1}{2} \frac{Q_{dis}^2}{E_{dis}} \right) / 0.5 \quad (3.11)$$

Areal capacitance is the capacitance per unit area (mF cm^{-2}), the working area is the geometric area immersed in the electrolyte which is 0.5cm^2 , V_{app} is the applied voltage in the cell (V).

Suppose in the cathodic test, the best voltage range is ΔV_c , and for the anodic test is ΔV_a , then its electrochemical window is $\Delta V(\Delta V_a + \Delta V_c)$, as shown in the figure 3.6, the principle of selection is the maximum potential range of the normal CVs without distortion and the coulombic efficiency is about 95% over entire charge/discharge cycles.

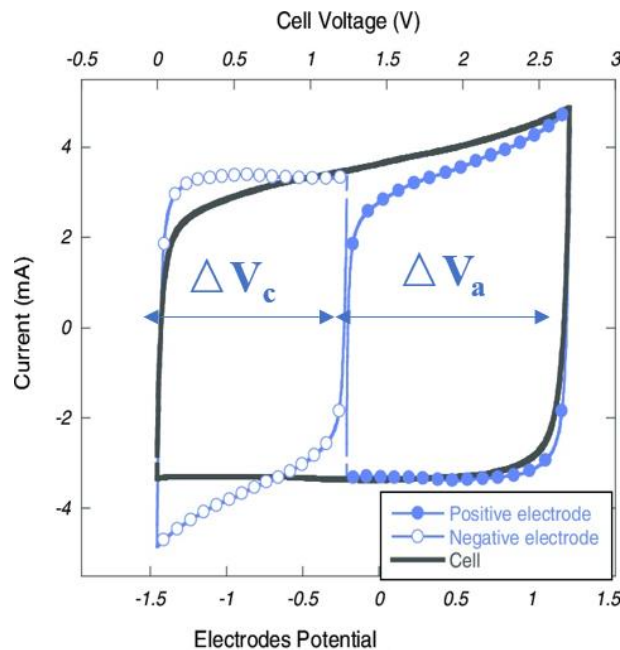


Figure 3.6 Anodic/cathodic test

(3) EIS

EIS is one of the most powerful tools for studying the electrochemical processes

occurring at the electrode/electrolyte interface. In the EIS test, the input signal is often a small amplitude sinusoidal AC signal, and then the impedance of the system is measured, to analyze the equivalent circuit. Impedance input and output signals have three characteristics, amplitude, frequency, and phase. Impedance is a complex number, which can be divided into two parts, the real part and the imaginary part. Therefore, the obtained EIS spectrum also takes these two parts as the Z' and Z'' , as can be seen in figure 3.7 [47], the EIS of general porous material is mainly composed of a semicircular ring in the high-frequency part and a vertical line in the low-frequency part. The X-axis (Z') is the real part and the Y-axis (Z'') is the imaginary part, the larger value in the X-axis direction, the lower the frequency. The high-frequency region of the semicircular capacitive reactance arc is dominated by electrochemical polarization (charge transfer), and the low-frequency region is dominated by concentration polarization (material transfer).

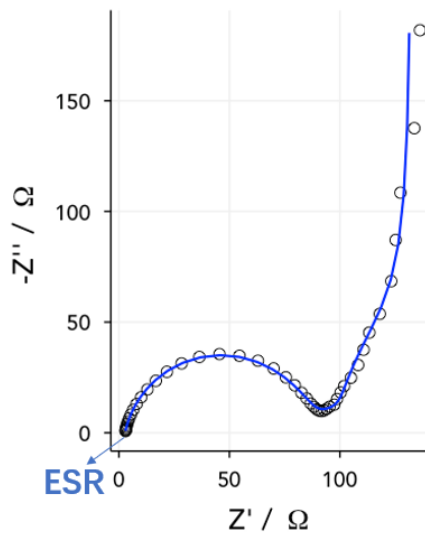


Figure 3.7 Nyquist plot

For our EIS experiments, the measurements are performed at open circuit voltage between 10mHz to 1MHz frequency range taking into account a 5mV rms sine-wave voltage amplitude, the electrode is measured under non-polarized conditions.

Figure 3.8 shows a three-electrode cell being tested on VPM3 to obtain EIS and CVs.

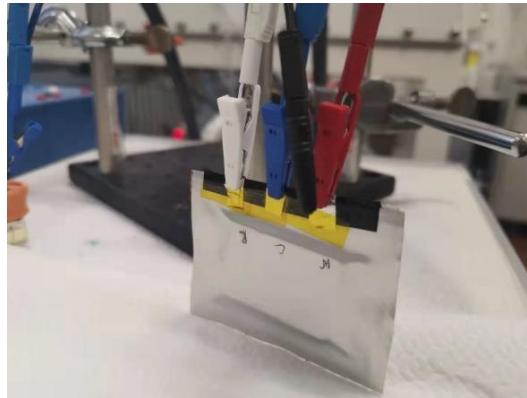


Figure 3.8 A three-electrode cell, the working electrode (anode) was connected to the red clip, the counter electrode(cathode) was connected to the blue clip, and the reference electrode was connected to the white clip.

(4) GCD

The GCD test, which is to charge and discharge the measured electrode or device under constant current conditions, record the change law of its potential or voltage with time, and study the law of potential change as a function of time. As can be seen in figure 3.9 [61], the potential changed at multiple current densities (with different colors), and storing-releasing time can be known: generally, decreasing storing-releasing time as the current density increase.

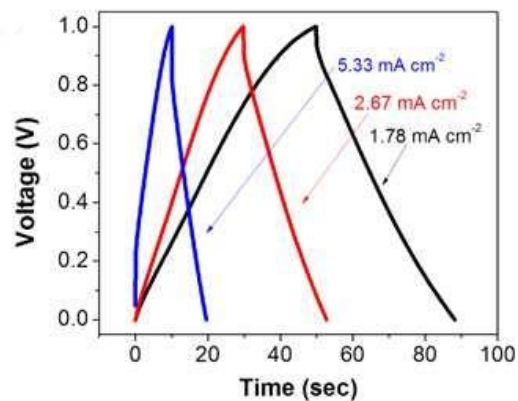


Figure 3.9 The change of voltage versus time [45]

When the electrode is charged to a certain constant potential for a long enough time, the electrode discharges when the supercapacitor starts to discharge and the potential has a dip voltage, called IR drop as shown in figure 3.10 and the relationship between ESR and IR drop is a larger (ESR) leads to a larger IR drop, the charging/ discharging efficiency of supercapacitor therefore decreases.

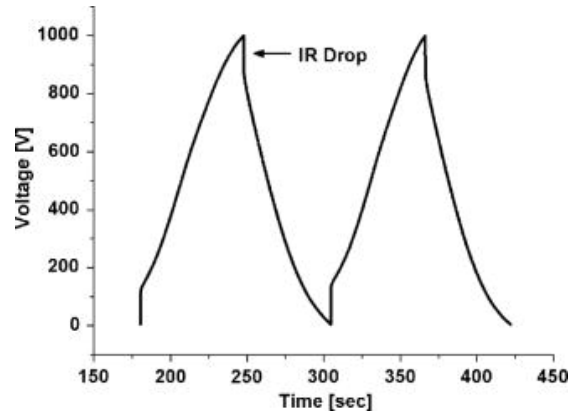


Figure 3.10 IR drop [63]

In our galvanostatic tests, maintain the current densities at $10\mu\text{A cm}^{-2}$, $20\mu\text{A cm}^{-2}$, $50\mu\text{A cm}^{-2}$, $100\mu\text{A cm}^{-2}$, $200\mu\text{A cm}^{-2}$ in each 500 charge/discharge cycles to measure electrochemical behavior (coulombic efficiency, energetic efficiency, and capacitance retention). Considering the activation time of electrodes in the first 500 charge/discharge cycles, the current condition is better changed to $10\mu\text{A cm}^{-2}$ after finishing 2500 cycles to obtain more accurate electrochemical performance.

Energetic efficiency (η_E) is the ratio of the discharging energy density and the charging energy density, the calculation of η_E is as follow:

$$\eta_E = \frac{E_{dis}}{E_{ch}} \quad (3.12)$$

CR (capacitance retention) is the ratio of the areal capacitance (specific capacitance) and the maximum areal capacitance (C_{max} , has a unit of mF cm^{-2}) over the entire charge/discharge cycles, and which is used to describe the degree of capacitance attenuation. The calculation of CR is as follow:

$$CR = \frac{C_{dis,S}}{C_{max}} \cdot 100 \quad (3.13)$$

(5) Float test

In float tests, holding the cell at the highest voltage which is 3V (electrochemical window) at a certain time (20h) in each float cycle, as shown in figure 3.11. In our experiment to measure the capacitance retention, energetic efficiency, coulombic efficiency of LIG supercapacitors over entire 25 float cycles (500h). If the capacitance retention maintains a high value in more cycles, the better the stability of electrodes and the longer lifetime of supercapacitors. Compared with the traditional CV test, the float test could show the degradation phenomenon that might occur during the electrochemical process.

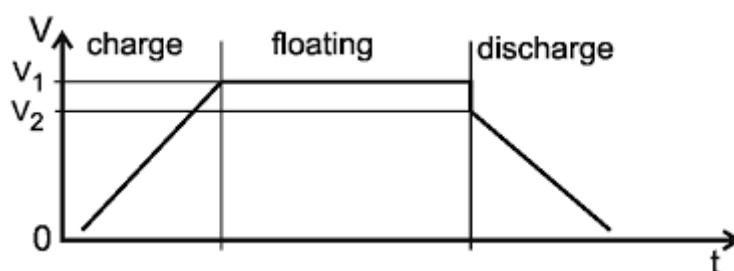


Figure 3.11 Float test [64]

3.5 Aim of study

In summary, porous graphene nanomaterials have high specific surface area, excellent electrical conductivity, and high chemical stability, they have great potential for development as supercapacitor electrodes. In addition, laser-induced graphene, as a technology that uses laser energy to convert various carbon-based materials into graphene, is a highly efficient, easy way to operate, and causes low pollution.

LIG supercapacitor is the main research object of this thesis, the preparation of electrode materials, the choice of electrolyte, and the assembly process affect the electrochemical performance of LIG supercapacitor: specific capacitance, energy

density, power density, and many others. In addition, this thesis studied an asymmetric LIG supercapacitor, the charge unbalancing caused by the asymmetrical structure which is a new challenge to be solved because balancing charges in order to exploit the maximum voltage and as we known from equation 3.3, 3.5, the larger voltage we obtain, the more energy and the more power we have of the LIG supercapacitor.

Chapter 4 Experimental

It has been carried out through a collaboration between the Department of Applied Science and Technology (DISAT) of Politecnico di Torino and Microla Optoelectronics s.r.l. and at the Chilab - Materials and Microsystems Laboratory of Chivasso (TO).

Firstly, comparing the effects of two IL electrolytes ([EMIM][TFSI] and [PYR14][TFSI]) on the electrochemical performance of LIG supercapacitors, CV, EIS and GCD were carried out on the electrochemical workstation (BioLogic), and all electrochemical tests were carried out at room temperature. In the previous sample preparation, there were several qualified samples under the same laser parameters, which means that assembled LIG supercapacitors under the same parameters could be used to team up for cathodic test and anodic test. By analyzing and comparing the results (specific capacitance, coulombic efficiency, energy density), selected a more suitable IL electrolyte to assemble the LIG supercapacitors whose graphene electrodes are printed under different selected laser parameters (15~18), and the cells were named by laser parameters.

Cell Name	Raster [dpi]	Power [%]	Frequency [kHz]	Velocity [mm/s]
15	400	19	5	375
16	400	19	5	400
17	400	19	5	425
18	400	19	5	450

Table 4.1 Tested cells

4.1 Comparison between [EMIM][TFSI] and [PYR14][TFSI]

The anions in the two different electrolytes are the same, so the size and arrangement of the cations have an important impact on the electrolyte, the structure of [EMIM]⁺, [PYR14]⁺ and [TFSI]⁻ are shown as below (figure 4.1) [60].

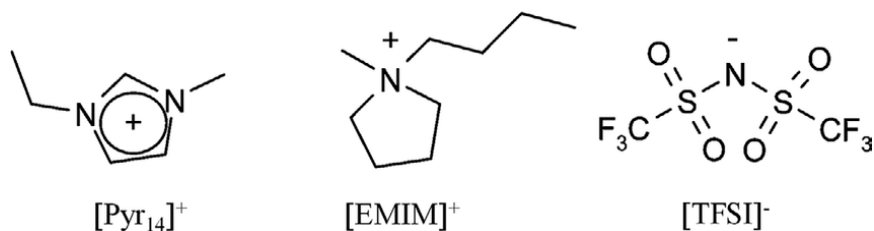


Figure 4.1 The structure of the electrolyte [EMIM]⁺, [PYR14]⁺ and [TFSI]⁻

The object of this experiment are cells 16 (laser parameters can be seen in table 4.1) which sheet resistances are small, using different ILs ([EMIM][TFSI] and [PYR14][TFSI]), which were measured by anodic test, cathodic test, and EIS test. The experimental results are shown in the figure 4.2, from the perspective of impedance, the impedance performance of different electrolytes in the anodic test and the cathodic test have the same behaviors, as seen in figure 4.2(a), From the enlarged view of EIS, the ESR of two ILs are different, almost 50Ω for [EMIM][TFSI] and [PYR14][TFSI] is about 100Ω which means [PYR14][TFSI] is more resistive, and observe the low-frequency region of EIS (the highest point of EIS), the value is relatively small under the effect of [PYR14][TFSI], at about 2300Ω, after changing [PYR14][TFSI] to [EMIM][TFSI], this value is twice as large. From figure 4.2(b), the upper limit of the voltage range selected in the anodic test is 1.2V, and for the cathodic test is 1.8V, so the intercepted electrochemical window is 3V. As can be seen, the areal capacitance increases with the increase of the voltage window, regardless of the cathodic test or the anodic test, [PYR14][TFSI] performs better than [EMIM][TFSI] in the same voltage range. For example, in the anodic test with a voltage window of 0.2V, the area capacitance of [PYR14][TFSI] can reach 1.9mF cm⁻² while [EMIM][TFSI] can only reach 0.9mF cm⁻² which proves [PYR14][TFSI] has a wider electrochemical window and higher ion mobility than [EMIM][TFSI].

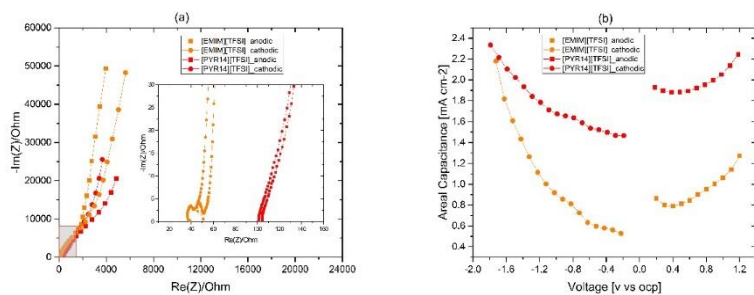


Figure 4.2 Electrochemical performance of two different ILs (a) shows the impedance performance of [EMIM][TFSI] and [PYR14][TFSI] in the EIS plot, fig(b) compares the areal capacitance between [EMIM][TFSI] and [PYR14][TFSI] at multiple different potential ranges.

4.2 Comparison of different devices using [PYR14][TFSI]

From the previous experiments, it can be concluded that [PYR14][TFSI] has a better electrochemical performance than [EMIM][TFSI] in LIG supercapacitors. Not only that, from the safety perspective, [EMIM][TFSI] is toxic and [PYR14][TFSI] is not. What's more, [PYR14][TFSI] can be production scalable, so in the following experiments, only [PYR14][TFSI] is used as the electrolyte to assemble devices. In this comparative experiment, the test objects are the cells 16,17,18 (table 4.1).

In theory, each device is subjected to cathodic test and anodic test, and the number of charge/discharge cycles reaches hundreds of times. As the number of cycles increases, the coulombic efficiency begins to slowly decrease after reaching a peak due to the influence of the reaction speed and IR drop. Even in the maximum voltage window, the CV formed by the charging/discharging process deviates seriously from the rectangle-like shape, and the coulombic efficiency has a cliff-like decline (generally appears when the coulombic efficiency is less than 95%). As seen in figure 4.3, the blue voltammogram and the red voltammogram are plotted to represent the box-shape of CVs. The potential range of cell 16 by applying cathodic test is 1.8V (figure 4.3(a)) compared with that of cells 17,18 (2V), which indicates the electrochemical window is

narrower. By looking at all the red voltammograms (figure 4.3(a), (b)), CVs are box-like shapes and the potential range is 1.2V for all devices under anodic test. In addition, the coulombic efficiency of the anodic test (above 95% at multiple potential ranges) performed better than the coulombic efficiency of the cathodic test.

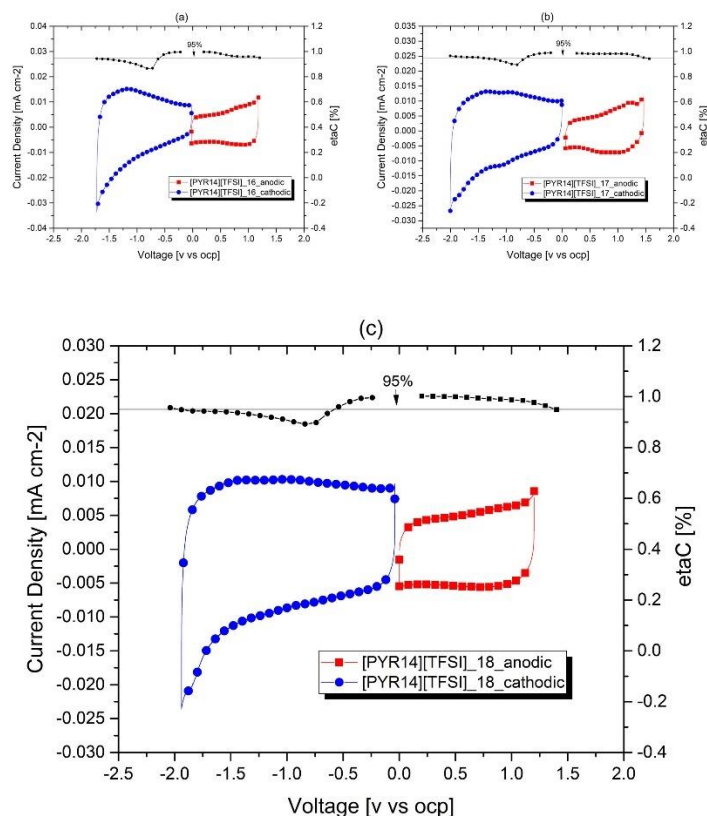


Figure 4.3 Electrochemical performance of three cells, (a), (b), and (c) are the electrochemical test diagrams of cells 16, 17, and 18 respectively, each figure integrates the CVs and coulomb efficiency curve under the anodic test and cathodic test. The red square curve in the figure represents the CVs of the anodic test, and the blue circular curve represents the CV curve of the cathodic test. In addition, there are two black curves at the top of the figure which represent the coulombic efficiency curve, to facilitate the reading, a reference line with a coulombic efficiency of 95% is set.

4.3 Oxygen effect on [PYR14][TFSI]

It can be seen from the coulombic efficiency curve of the cathodic test that there is a strange phenomenon in the trend of the curve, that is, the coulombic efficiency decreases slowly from the beginning, then suddenly drops for a while and then slowly rises later, and a low-lying shape appears in the first half of the curve. The reason for this phenomenon is oxygen contamination, since the preparation process of LIG supercapacitors were completed in the dry room and the packaging were completed in a vacuum environment, the entire preparation process only lasts 30mins. Excluding the oxygen introduced during the preparation process, the only possibility is that the IL [PYR14][TFSI] placed in the dry room for a long time, the storage container was not completely sealed and it was exposed to the air every time when it was used, resulting in oxygen reduction reaction occurred on the surface of carbons. The effect in the CV curve is that the reduction current becomes smaller, by equations 3.7, 3.10, coulombic efficiency decreases accordingly.

To prevent oxygen from dissolving in the electrolyte, the electrolyte is vacuum-packaged after each usage. For the convenience of distinction, [PYR14][TFSI] without vacuum packaged is defined as old [PYR14][TFSI], on the contrary, the vacuum packaged [PYR14][TFSI] is defined as new [PYR14][TFSI], as shown in figure 4.4.



Figure 4.4 Vacuum packaged [PYR14][TFSI]

In this experiment, cells 17 and 18 are used for testing to compare ESR, areal capacitance and coulombic efficiency when using the old and the new [PYR14][TFSI]. It can be seen in figure 4.5(a), (c) that reducing the amount of oxygen dissolved in the electrolyte can reduce the contact impedance between the electrolyte and the electrode on the one hand. The ESR of the cell 18 has been reduced from the previous 120Ω to 66Ω and the ESR of cell 17 has also been greatly reduced, from 123Ω to 76Ω . On the other hand, in any voltage sweep range, the areal capacitance has a large increase in anodic test or cathodic test, as shown in figure 4.5(b), (d), for the cathodic test of cell 18, the areal capacitance reaches 1.6mF cm^{-2} when the voltage range is 1.8V , and the areal capacitance reaches 2.4 mF cm^{-2} based on the new electrolyte under the same premise, the increase is up to 60% similarly, the areal capacitance of cell 17 has increased by 53%.

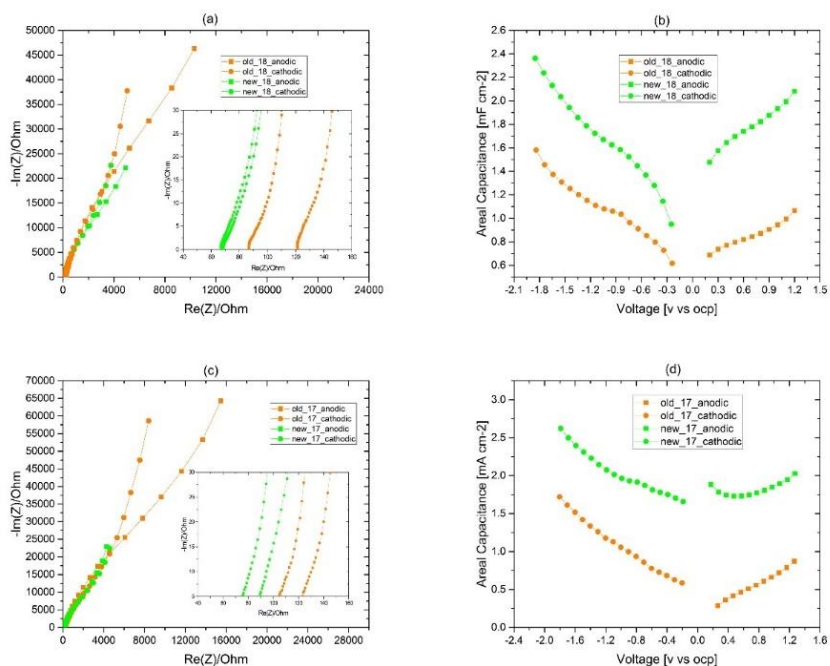


Figure 4.5 Electrochemical performance of new and old [PYR14][TFSI], (a) and (c) are the EIS plots of cells with old and new [PYR14][TFSI], and the enlarged view of the high-frequency region of EIS. (b) and (d) are the graphs of the change of the areal capacitance of cells 18 and 17 with the voltage range, respectively. They are also compared under the new (green curve) and old (orange curve) [PYR14][TFSI].

It can be seen from the figure 4.6 that although the coulombic efficiency curve still has a "sag" phenomenon, the "sag" has been significantly improved after the vacuum packaged [PYR14][TFSI] is used. For cells 17 and 18, using electrolyte contaminated by oxygen, the minimum values of the coulombic efficiency curve are 89.5% and 89.2% by applying cathodic test. After improving the storage method of the electrolyte, the minimum value of the coulombic efficiency curve is increased to 92.3% and 93.2% respectively. In addition, the benefit of the new [PYR14][TFSI] is that in the process of gradually increasing the measurement voltage range, the coulombic efficiency exceeds 95% in more charge/discharge cycles which means the stability of the cell is improved.

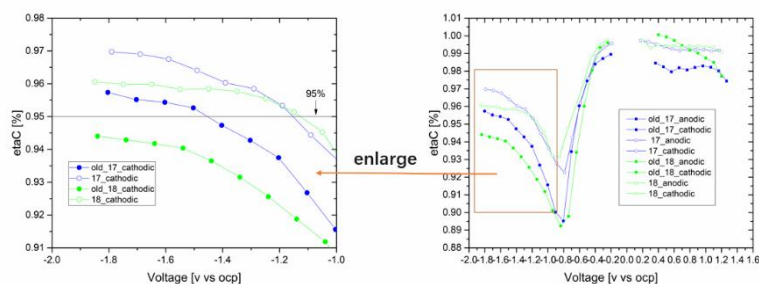


Figure 4.6 Enlarged view of coulombic efficiency curve shows the curve of the coulombic efficiency as the voltage range changes. Here are eight curves for cells 17, 18 with old and new [PYR14][TFSI] under anodic/cathodic test. The left side of the figure is a partial enlarged view of the cathodic test and round icons for all curves. The solid round icon represents the old [PYR14][TFSI], the hollow round icon represents the new one, the blue curve represents device 17 and the green curve represents device 18. Here is also a reference line with a coulombic efficiency of 95%.

4.4 Select the most appropriate laser parameters

As seen in figure 4.7, when measuring cells (15~18) under anodic and cathodic test, the voltage of working electrode (related to the voltage of reference electrode, V_{ref}) and the voltage of counter electrode (related to V_{ref}) change with time, the voltage of the counter electrode (purple, red lines) is much smaller than the voltage of the working electrode (blue, green lines) both in anodic test and cathodic test, and the drift of voltage of the counter electrode can be negligible. This could be a proof that the LIG pseudoref is quite stable when measuring and the electrical parameters we obtain are reliable.

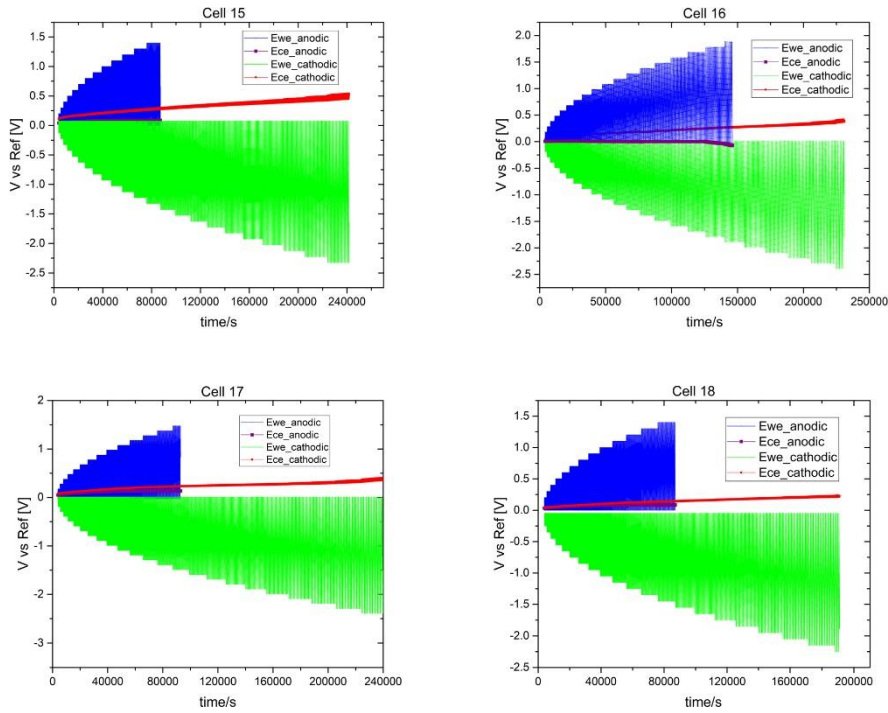


Figure 4.7 The drift of counter electrode

Re-preparation of cells 15~18, without changing the previous measurement tools and methods, compare the Nyquist plot, CVs and coulombic efficiency curve of the four devices. In addition, for each device, the cathodic test and anodic test are paired, these two tests give two areal capacitances. In the simulation circuit, the two capacitors are connected in series, so the total equivalent capacitance (C_{eq} has a unit of mF cm^{-2}) can be expressed as equation 4.1:

$$C_{eq} = \frac{C_a \cdot C_c}{C_a + C_c} \quad (4.1)$$

C_a is anodic capacitance (mF cm^{-2}) and C_c is cathodic capacitance (mF cm^{-2}).

With increasing charge/discharge cycles, figure 4.8. shows the orange voltammogram (400 cycles) with respect to the sickle-like CV of devices, the reduction current quickly decreases in the reverse scan, which means the operating potential window (2V) is larger than the real cell potential by applying cathodic test causes poor electrochemical performance. The maximum electrochemical potential window by

looking at the red voltammogram (340 cycles, the potential range is 1.8V), CVs are rectangular-like shape and it could be concluded that the coulombic efficiency is higher than in other potential windows (more than 340 cycles). By knowing the maximum potential range is 1.2V (the same for all cells), which is measured by the anodic test, thus, the electrochemical potential window is 3V for each cell.

It can be seen from figure 4.9. the electrochemical performance of devices in the anodic test is not much different, while in the cathodic test, the shape of the CVs (figure 4.9(a), (d)) is a rectangle-like shape, so it can be inferred that the coulombic efficiency of these two devices is higher than that of the other two devices in the operating potential window. For cell 15 (figure 4.9(a)), its coulombic efficiency is above 95% over the entire potential window, in contrast, the coulombic efficiencies of other devices are temporarily lower than the reference line (coulombic efficiency 95%).

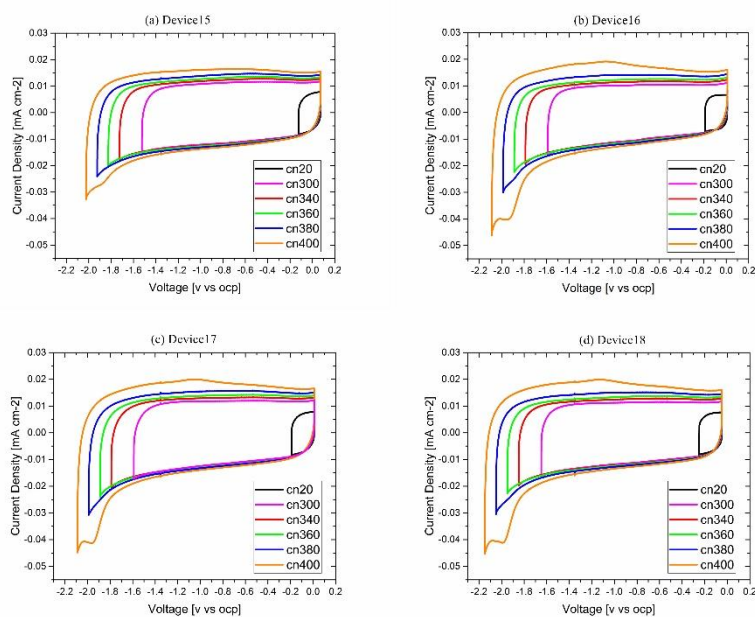


Figure 4.8 Cyclic voltammetry under cathodic test at multiple charge/discharge cycles: 20 cycles (black line), 300 cycles (pink line), 340 (red line), 360 (green line), 380 (blue line), 400 (orange line) of (a) cell 15, (b) cell16, (c) cell17 and (d) cell18.

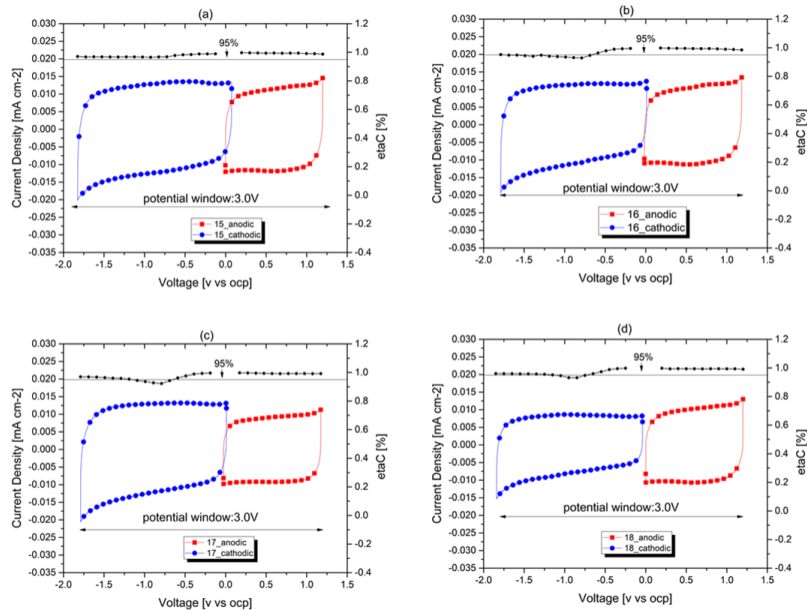


Figure 4.9 Electrochemical performance of four cells, (a), (b), (c), (d) are the double Y plots of cells 15, 16, 17, 18 respectively, CVs and coulombic efficiency curve are shown in one figure, the red square curve is the result under the anodic test while the blue circular curve is the result under the cathodic test. Similarly, set a reference line with a value of 95% on the coulombic efficiency curve.

First of all, it can be observed from figure 4.10. that the impedance of cell 16 and cell 18 is more stable. It is intuitively shown that the two EIS curves in the cathodic test and the anodic test are closer, which means the response of ESR varies with frequency in these two tests are the same. The ESR of cells 17, 18 is much smaller than that of the other two cells which means these two cells are less resistive. The two ESR values of cell 18 are approximately 67Ω , but the two ESR values of the cell 17 are slightly different which is normal. After a comprehensive comparison, it can be found that cell 18 performs the best in terms of impedance.

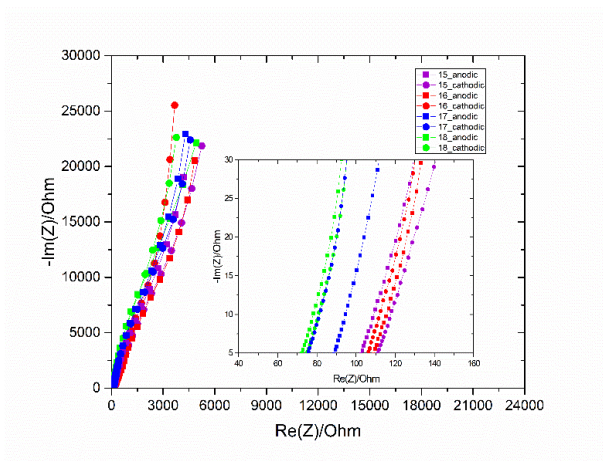


Figure 4.10 Nyquist plot of four devices

Then C_{eq} of cells 15~18 can be calculated by equation 4.1, as can be seen from table 4.2, according to C_{eq} , the order from largest to smallest is cell 18, 15, 16, 17. In summary, it can be concluded that cell 18 has the advantages of high capacitance and low impedance which brings high power and high energy. Because of the largest C_{eq} (0.63mF cm^{-2}) of cell 18, in the following tests only tested cell 18.

Cell Name	Ca [mF cm-2]	Cc [mF cm-2]	Ceq [mF cm-2]	Positive voltage [V]	Negative voltage [V]
15	0.97	1.73	0.62	1.2	1.8
16	1.07	1.36	0.60	1.2	1.8
17	0.87	1.67	0.57	1.2	1.8
18	1.06	1.58	0.63	1.2	1.8

Table 4.2 The equivalent capacitance

4.5 Optimize charge balancing

From the results of the preliminary experiment, in different ILs, [PYR14][TFSI] has outstanding electrochemical and physical properties. In the subsequent experiments, the troubles caused by oxygen contamination were also solved in the form of vacuum packaging. Therefore, in this section, vacuum-packaged [PYR14][TFSI] is used as an electrolyte to prepare LIG supercapacitors in all the experiments.

The experiment contents are as follow:

(1) According to the comparison results, select the device with the best electrochemical performance (generally C_{eq} is the maximum among all devices) to calculate the area ratio, which is the value between two interdigital part surface areas, which can be expressed as the equations as below:

$$Q_c = C_c \cdot \Delta V_c \quad (4.2)$$

$$Q_a = C_a \cdot \Delta V_a \quad (4.3)$$

$$\Sigma_+ \cdot C_a \cdot \Delta V_a = \Sigma_- \cdot C_c \cdot \Delta V_c \quad (4.4)$$

$$M_+ = \frac{\Sigma_+}{\Sigma_-} = \frac{C_c \cdot \Delta V_c}{C_a \cdot \Delta V_a} \quad (4.5)$$

ΔV_c is cathodic voltage range (V), ΔV_a is anodic voltage range (V), Q_c is the cathodic charge per unit area, Q_a is the anodic charge per unit area, Σ_+ is the anodic surface area (cm^2), Σ_- is the cathodic surface area (cm^2) and M_+ is area ratio.

Since the experimental object is an asymmetric supercapacitor, the electrode polarization in the cathodic test and the anodic test is asymmetrical, resulting in different amounts of charge per unit area measured by these two tests (Q_a is not equal to Q_c). To optimize charge balancing of cathode and anode, the area ratio should be adjusted according to the actual amount of charge. It is worth noting here that the two electrodes of interdigitate structure were made of the same active material. There is no difference except the surface area, so the area ratio is the mass ratio or volumetric ratio. On the basis of the equation 4.5 to calculate M_+ , then redesign the mask according to this ratio.

In general, there are three ways to design a mask. Keep the area of one side of the

interdigit the same as the original mask, adjust the length and width ratio of the other side of the interdigit to make the area ratio of both sides of the interdigit approach the theoretical value: 1) keep constant length, change width; 2) keep constant width, change length; 3) change length and width at the same time.

Use laser etching machine to transfer the designed mask pattern to a 100 μ m steel sheet through laser parameters controlled by computer, this step was completed in Microla company, then use the same laser parameters as the selected device to print the samples with those new masks.

4.5.1 Redesign masks

Prior to printing, the design of new masks has become an inevitable step to improve the electrochemical performance of asymmetric supercapacitors due to charge unbalancing between the two electrodes. On the basis of the equation 4.5, the optimal area ratio between the two electrodes was measured as 2.24, which is obviously the original mask is no longer suitable to print devices for the charge unbalancing. The device we fabricated composed of 6 digits and 5 digits, it is indicated the area ratio of the original mask is 1.2, it is necessary to increase the area ratio from 1.2 to 2.24, which can be achieved by shortening the width or the length of 5 digits, in the meanwhile, keep the area of 6 digits unchanged. The figure 4.11 indicates width is 0.6cm and length is 4.5cm of 6 digits, figure 4.11(a) shows the width was shortened to 0.27cm and figure 4.11(b) shows an alternative way to obtain the desired area ratio, only change the length from 4.5cm to 2.4cm. The most complex method as shown in figure 4.11(c), there are countless combinations of changing length and width at the same time, and one of them was shown here (the length was shortened to 2.97cm and the width was shortened to 0.6). The three mask patterns designed have the same area ratio, hence, which were named mask1, mask 2, and mask 3 in the order of the figure (a),(b) and (c) while the original mask was named mask 0.

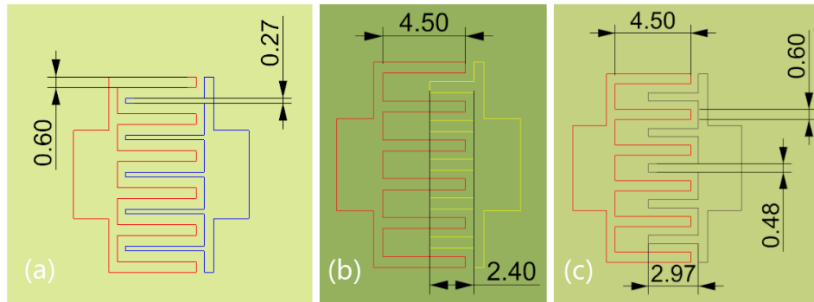


Figure 4.11 Redesign masks in three ways

However, considering the limitations of laser printing, it is difficult to transfer the pattern of mask1 to the steel sheet. From a practical point of view, after laser cutting the steel sheet, the pattern needs to be peeled off from the steel sheet, and a certain width of maks1 is only 0.27cm, the pattern is easily damaged due to the stress of the detached process. What's more, when LIG printing through the mask, generally, the smaller the pattern, the narrower the acceptable error range, undoubtedly, it improves the difficulty of the operation and the requirements for LIG printing. Therefore, the design of mask 1 was rejected.

Appropriate laser parameters are crucial for laser cutting, the required laser energy depends on the material type and thickness and the laser energy is determined by the laser parameters controlled by computer. Most importantly, laser energy relates to whether the designed pattern can be completely cut, and whether the edges of the pattern are sharp and tidy. Before cutting the mask pattern, used the laser parameters (table 4.3) to cut a 10mm long straight line with a 100 μ m steel sheet for practice. The operating environment and the laser machine (infrared pulse continuous wave at 10.6 μ m wavelength) as shown in figure 4.12 and the results of laser cutting in a steel sheet.

Sample Name	Current [A]	Frequency [kHz]	Velocity [mm/s]	Repetitions
1	30	30	30	1
2	30	30	30	20
3	30	30	30	40
4	30	30	30	80
5	30	30	30	160
6	30	30	30	320

Table 4.3 Experimental laser-cutting parameters

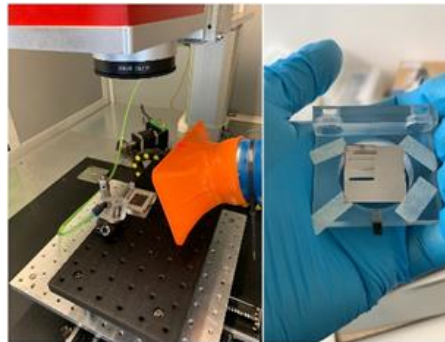


Figure 4.12 Laser cutting straight lines

Figure 4.13 showed the morphology of these six straight lines with different repetitions via optical microscope imaging. Increased laser cutting repetitions from figures 4.13(a) ~ (f), it is clear that the energy from laser cutting caused dramatic changes in steel sheet and as the repetition of laser cuts increased, the straight line was slowly cut out from the steel sheet. Turned on the light source of the microscope and observed the figures 4.13(a)~(c) showed that the light source cannot pass through the linear gap on the steel sheet but the straight line could be completely cut with repetitions above 80 (figure 4.13(d)~(f)), it was noticeable that the morphology of straight line was not perfect (the cut edges were uneven) with repetitions 80 or 160. When the repetitions of laser cutting increased to 320, the result of cutting was the most ideal as shown in figure 4.13(f).

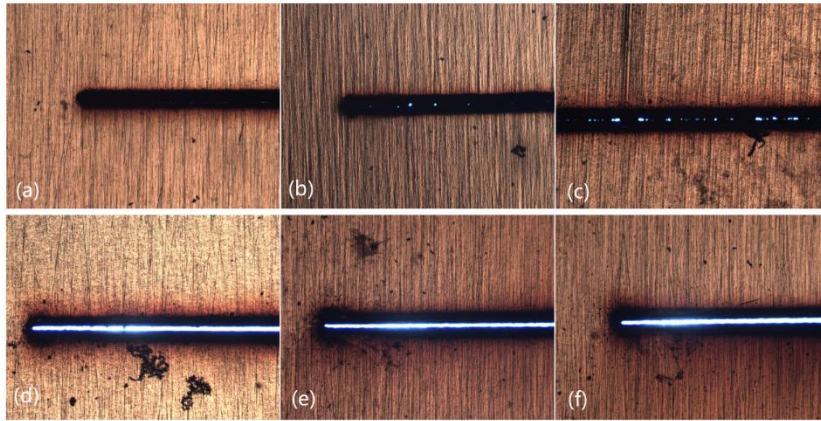


Figure 4.13 The morphologies of laser-cutting straight line were observed by the optical microscope, (a)~(f) corresponding to lines 1~6.

Laser cutting the pattern of masks 2,3 with selected laser parameters, each cutting time lasted 30mins, placed the blower inside to prevent the overheat generated by the laser energy from bending the steel sheet in the laser writing process. Then cleaned masks in an ultrasonic bath with a 3-min step in acetone and were dried under wind flow to ensure acetone evaporated completely.

The same process to print LIG electrodes and fabricate LIG supercapacitors, measured electrochemical behavior by employing different methods in the Arbin instrument (no longer measured by applying cathodic test and anodic test), as shown in figure 4.14, a cell being tested in Arbin instrument for the GCD test and the float test.

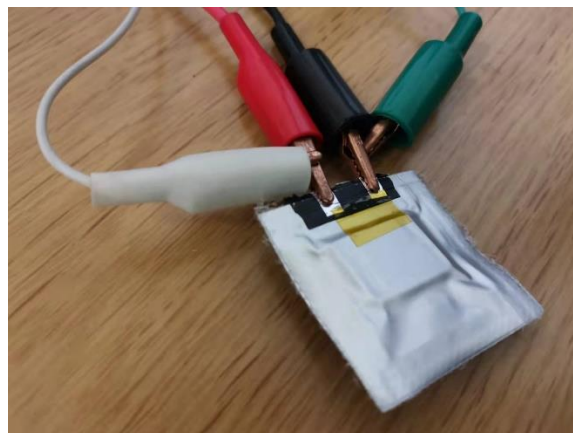


Figure 4.14 The connection way of GCD/float test

From the charge/discharge cycles, as can be seen in figure 4.15, the reaction time of mask 0 was shorter, almost reached a stable state after the first 500 cycles, and the coulombic efficiency was as high as 99.7%. The coulombic efficiencies showed mask 2, mask 3 have bad performances, by increasing current densities, the coulombic efficiency increases and jitter appeared in the arising process which means the stability of these two masks was worse than mask0. In addition to coulombic efficiency, the same behavior for energetic efficiency by looking at the figure 4.15(b), but the strange phenomenon was that the energetic efficiency sharply decreased of cell (mask 0) when the current density increased to $50\mu\text{A cm}^{-2}$, also was the minimum coulombic efficiency compared with cell (mask 2) and cell (mask 3) which proved the cell (mask 0) was more resistive. The coulombic efficiency and capacitance retention of cell (mask0), in contrast, were higher than the other cells over the entire charge/discharge cycles. By observing figure 4.15(a), (c), the coulombic efficiency was not related to the capacitance retention and energetic efficiency.

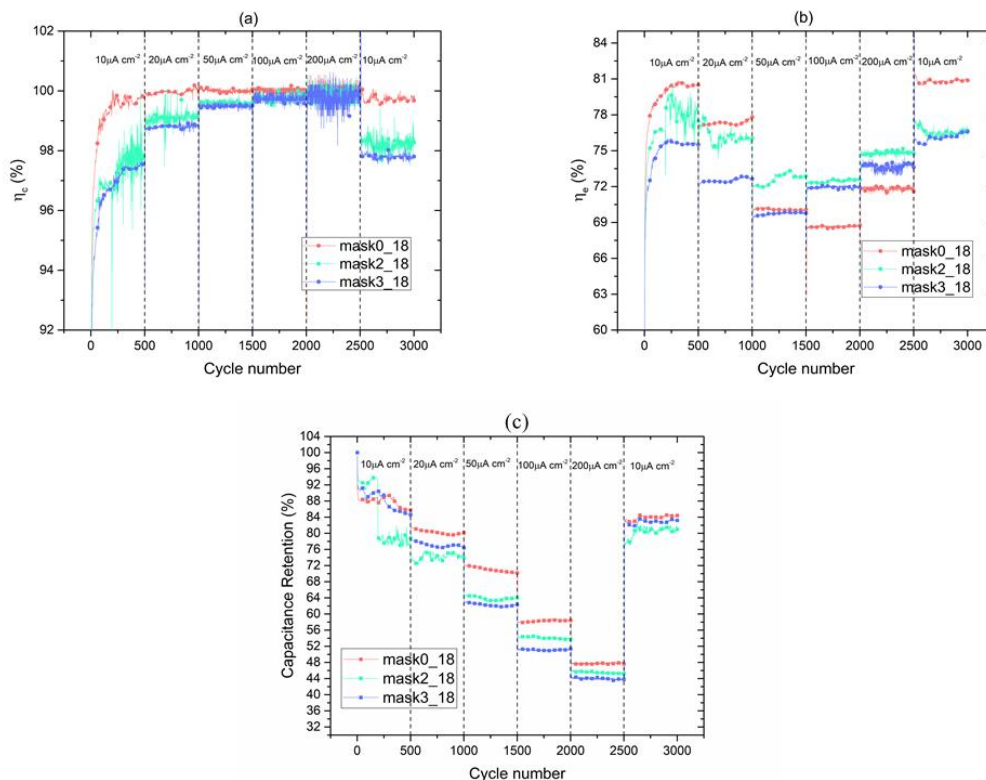


Figure 4.15 GCD test of three cells, (a) Compare the coulombic efficiency of three cells whose

LIG electrodes were printed through mask0 (orange line), mask2 (green line), mask3 (blue line) at multiple current densities. (b) energetic efficiency and (c) capacitance retention.

From the GCD test, ragone plot was computed as shown in figure 4.16. The best cell (mask 0) and the worst cell (mask 2), the areal energy does not decrease too much since voltage was kept constant between the two. But as can be seen from coulombic efficiency and energy efficiency, the optimized device behaves better for the same energetic performances.

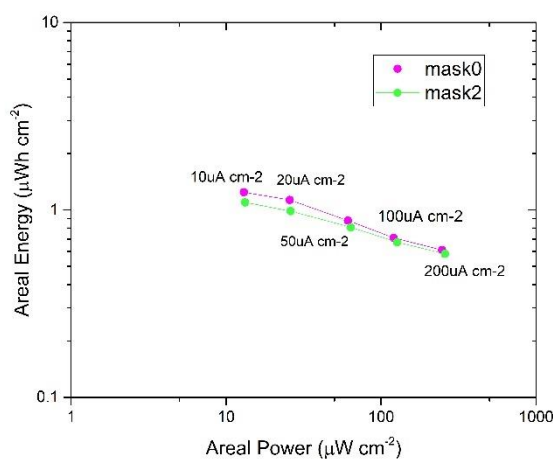


Figure 4.16 Ragone plot of two cells

Judging from the key parameters of coulombic efficiency, energetic efficiency and capacitance retention, the results of the experiment did not meet expectations (the original area ratio is closer to the optimized one). Taking into account the uncertainty of the laser instrument and the preparation environment, we decided to re-evaluate the area ratio of cell 18, this time we fabricated two cells 18 to obtain the average area ratio to ensure validity and reliability. One cell is 1.7, the other cell is 1.2, so the average area ratio is 1.45. From the comparison of the green curve and the blue curve in the figure 4.15, even though the area ratios are the same of two re-designed masks, it can be seen that mask 2 performed better than mask 3 in energetic efficiency and capacitance retention. Thus, in the design of the mask selection method, it is biased to only change

the length ratio of the digits to reach the desired area ratio. The change of one order of magnitude could affect the optimization of charge balancing, seven masks with different area ratios are shown in figure 4.17, from left to right are masks with the area ratio 1, 1.1, 1.3, 1.4, 1.5, 1.6, 1.7. In particular, there is a mask with the area ratio of 1.0, which is an asymmetrical structure, and the electrochemical behavior of symmetric supercapacitors and asymmetric supercapacitors could be compared.



Figure 4.17 Seven new masks

4.5.2 Results

New cells were named by their area ratio, figure 4.18(a) showed except for the brown voltammogram (symmetric cell), the other voltammograms with respect to box-like CVs. The areal capacitance in figure 4.18(b) indicated the brown line fluctuated greatly over entire charge/discharge cycles even though the areal capacitance was higher than the other cells. Excluding the brown line, the areal capacitance of the blue line (R1.4) was the highest. It was interesting to note the coulombic efficiency in figure 4.18(c), which gave a conclusion that the brown line had the worst behavior, in contrast, the blue, yellow and red lines reached higher coulombic efficiency (98.1%, 97.9%, 98.1%, respectively) after 100 charge/discharge cycles. In summary, asymmetric supercapacitors had better electrochemical performance than symmetric supercapacitors and the asymmetric cell (R1.4) had excellent behavior among all cells.

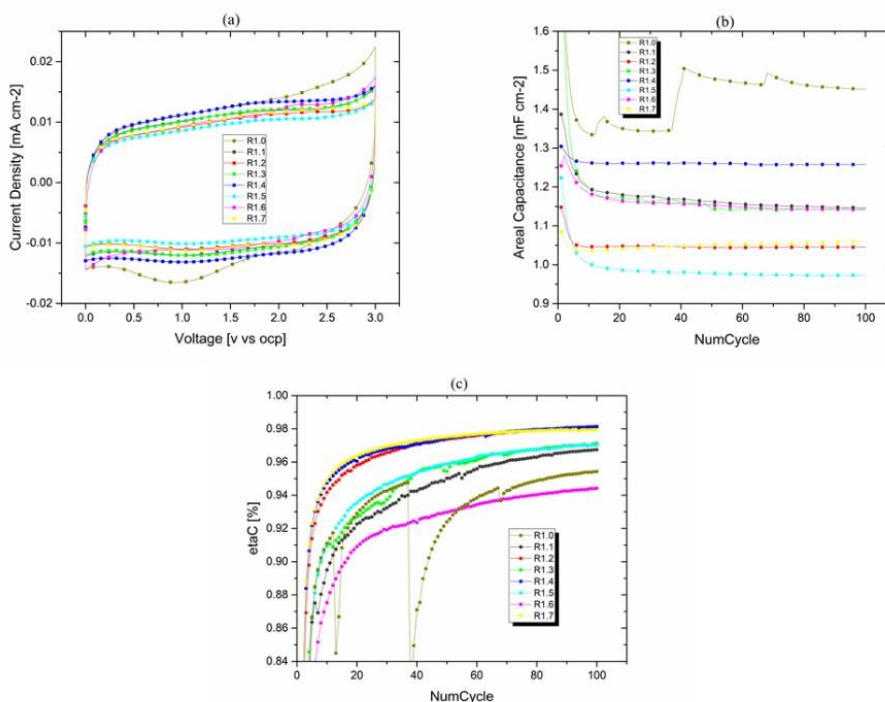


Figure 4.18. Electrochemical behavior of eight cells with different area ratio 1.0~1.7 (brown, grey, red, green, blue, light blue, pink and yellow line, respectively) by (a) cyclic voltammetry, the operating potential window is 3V, (b) the areal capacitance at 100 charge/discharge cycles and (c) coulombic efficiency.

Further compared the electrochemical performance among the selected cells 18 (R 1.4), an symmetric cell (R 1.0) and an asymmetric cell (R 1.3), as can be seen in figure 4.19, the blue line (R 1.4) had the best performance in coulombic efficiency (99.1%) and energetic efficiency (80.1%) compared with brown line (R1.0) and green line (R1.3). This experimental result accorded with the conclusion of the previous experiment: the energy, power and capacitance of asymmetric supercapacitors were higher than that of symmetric supercapacitors (figure 4.19(a)~(c)). Finally, the area ratio was changed from 1.2 to 1.4 could successfully optimize the charge balance and improve the cycle stability after 25 float cycles (500 hours) because the capacitance retention of (R1.4) could keep 98.8% at the last float cycles while (R 1.0) is only 96.6%.

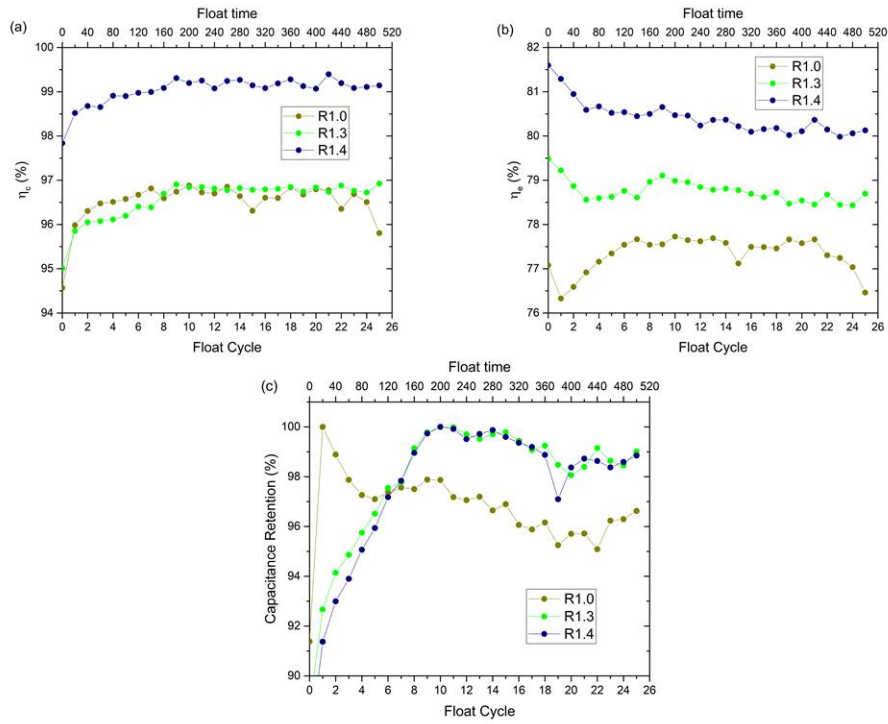


Figure 4.19 Float test of three cells. Comparison of the electrochemical behavior of three cells with the area ratio 1.0 (brown line), 1.3 (green line), 1.4 (blue line) by (a) coulombic efficiency in 1300 charge/discharge cycles at constant potential 3V (b) energetic efficiency (c) capacitance retention.

Chapter 5 Conclusions

The key novelty in this study was the use of an easy, time-saving method to produce electrodes of supercapacitors by laser-induced graphene (LIG) technique and did some research about the effects of the laser parameters on the sheet resistance of LIG and it was shown that minimize sheet resistance is beneficial to improve physical-chemical properties of LIG supercapacitors. Using the optimized laser-writing parameters (15~18), we prepared a metallic mask to print interdigitated supercapacitor electrodes on the polyimide foil. Firstly we fabricated LIG supercapacitors with two different ILs ([EMIM][TFSI] and [PYR14][TFSI]) and compared them by applying OCV test, CV (anodic and cathodic) tests, EIS test, it was showed that [PYR14][TFSI] had better electrochemical behavior than [EMIM][TFSI] and we found the oxygen affected on [PYR14][TFSI], to avoid oxygen contamination we used vacuum packaged [PYR14][TFSI] which improved the areal capacitance than the previous [PYR14][TFSI]. Then selected the best cells (cell 18) among cells (15~18) by the key electrical parameters (C_{eq}), but the problem of charge unbalancing caused by the asymmetrical structure of electrodes. To solve this problem, varied the area ratio of electrodes by redesigning masks (the area ratio of the original mask is 1.2). We fabricated new cells with designed new masks (area ratio from 1.0 to 1.7, the desired area ratio is 1.4) and measured electrochemical performance by applying GCD test to observe the influence on the electrical parameters (the coulombic efficiency, energetic efficiency and capacitance retention) of LIG supercapacitors. As a result, cell (R 1.4) reached the highest coulombic efficiency (98.1%) at multiple current densities. Selected the best cell (R 1.4), a symmetric cell (R 1.0) and an asymmetric cell (R 1.3) to do the float test. The results of this work, cell (R 1.4) was demonstrated could fix the problem of charge unbalancing and improve cycle stability by looking at the capacitance retention could keep (98.8%) which is higher than the other cells after 25 float cycles.

Bibliography

- [1] Peng Tiandang." Research on the Application of Supercapacitor in solar Power System of Buoy." *Journal of Mechanical & Electrical Engineering* 06(2011):62-64.
- [2] Kouchachvili, Lia, Wahiba Yaïci, and Evgueniy Entchev. "Hybrid battery/supercapacitor energy storage system for the electric vehicles." *Journal of Power Sources* 374 (2018): 237-248.
- [3] Helmholtz H. Studien über electriche Grenzsichten. *Annalen der Physik*[J].1879, 243(7): 337- 382.
- [4] Yang Shengyi, and Wen Fang. "Overview of Super Capacitors." *Modern Machinery* 4 (2009): 82-84.
- [5] Sprong M, Becker H E, Schothorst P F, et al. Pathways to psychosis: A comparison of the pervasive developmental disorder subtype multiple complex developmental disorder and the "At Risk Mental State". *Schizophrenia Research*[J]. 2008, 99(1-3): 38-47.
- [6] Wen, Xiaonan, et al. "Seedless synthesis of patterned ZnO nanowire arrays on metal thin films (Au, Ag, Cu, Sn) and their application for flexible electromechanical sensing." *Journal of Materials Chemistry* 22.19 (2012): 9469-9476.
- [7] Vangari, Manisha, Tonya Pryor, and Li Jiang. "Supercapacitors: review of materials and fabrication methods." *Journal of Energy Engineering* 139.2 (2013): 72-79.
- [8] Wang, Zhong Lin. "Toward self-powered sensor networks." *Nano Today* 5.6 (2010): 512-514.
- [9] Wang, Zhong Lin. "Self-powered nanosensors and nanosystems." (2012): 280-285.
- [10] Wang, Zhong Lin, and Wenzhuo Wu. "Nanotechnology-enabled energy harvesting for self-powered micro-/nanosystems." *Angewandte Chemie International Edition* 51.47 (2012): 11700-11721.
- [11] J. Gubbi, R. Buyya, S. Marusic, M. Palaniswami Fut. *Gener. Comput. Syst.*, 29 (2013), pp. 1645-1660
- [12] Beidaghi, Majid, and Yury Gogotsi. "Capacitive energy storage in micro-scale devices: recent advances in design and fabrication of micro-supercapacitors." *Energy & Environmental Science* 7.3 (2014): 867-884.
- [13] Hu, Haibo, Zhibin Pei, and Changhui Ye. "Recent advances in designing and fabrication of planar micro-supercapacitors for on-chip energy storage." *Energy Storage Materials* 1 (2015): 82-102.
- [14] Zhang, Hongxi, et al. "Recent advances in micro-supercapacitors." *Nanoscale* 11.13 (2019): 5807-5821.
- [15] Pan H, Li J Y, Feng Y P. Carbon nanotubes for supercapacitor[J].*Nanoscale Research Letters*, 2010, 5:654–668

- [16] Rogers, John A., Takao Someya, and Yonggang Huang. "Materials and mechanics for stretchable electronics." *science* 327.5973 (2010): 1603-1607.
- [17] Lipomi, Darren J., and Zhenan Bao. "Stretchable, elastic materials and devices for solar energy conversion." *Energy & Environmental Science* 4.9 (2011): 3314-3328.
- [18] Peng, Xu, et al. "Two dimensional nanomaterials for flexible supercapacitors." *Chemical Society Reviews* 43.10 (2014): 3303-3323.
- [19] Wu, Zhong-Shuai, Xinliang Feng, and Hui-Ming Cheng. "Recent advances in graphene-based planar micro-supercapacitors for on-chip energy storage." *National Science Review* 1.2 (2014): 277-292.
- [20] Han, Yan, et al. "Recent progress in 2D materials for flexible supercapacitors." *Journal of energy chemistry* 27.1 (2018): 57-72.
- [21] Yun, Junyeong, et al. "Stretchable patterned graphene gas sensor driven by integrated micro-supercapacitor array." *Nano Energy* 19 (2016): 401-414.
- [22] <https://passive-components.eu/tiny-bio-supercapacitor-provides-energy-for-biomedical-applications/>
- [23] http://nobelprize.org/nobel_prizes/physics/laureates/2010/
- [24] Lee, Changgu, et al. "Measurement of the elastic properties and intrinsic strength of monolayer graphene." *science* 321.5887 (2008): 385-388.
- [25] Bolotin, Kirill I., et al. "Ultrahigh electron mobility in suspended graphene." *Solid state communications* 146.9-10 (2008): 351-355.
- [26] Balandin, Alexander A., et al. "Superior thermal conductivity of single-layer graphene." *Nano letters* 8.3 (2008): 902-907.
- [27] Stoller, Meryl D., et al. "Graphene-based ultracapacitors." *Nano letters* 8.10 (2008): 3498-3502.
- [28] Lee, Changgu, et al. "Measurement of the elastic properties and intrinsic strength of monolayer graphene." *science* 321.5887 (2008): 385-388.
- [29] Huang, Jialiang, et al. "Scalable production of few layered graphene by soft ball-microsphere rolling transfer." *Carbon* 154 (2019): 402-409.
- [30] Berger, Claire, et al. "Ultrathin epitaxial graphite: 2D electron gas properties and a route toward graphene-based nanoelectronics." *The Journal of Physical Chemistry B* 108.52 (2004): 19912-19916.
- [31] Li, Dan, et al. "Processable aqueous dispersions of graphene nanosheets." *Nature nanotechnology* 3.2 (2008):

101-105.

- [32] Chen, Jianyi, et al. "Oxygen-aided synthesis of polycrystalline graphene on silicon dioxide substrates." *Journal of the American Chemical Society* 133.44 (2011): 17548-17551.
- [33] Li, Xuesong, et al. "Large-area synthesis of high-quality and uniform graphene films on copper foils." *science* 324.5932 (2009): 1312-1314.
- [34] Somani, Prakash R., Savita P. Somani, and Masayoshi Umeno. "Planer nano-graphenes from camphor by CVD." *Chemical Physics Letters* 430.1-3 (2006): 56-59.
- [35] Meyer, Jannik C., et al. "Imaging and dynamics of light atoms and molecules on graphene." *Nature* 454.7202 (2008): 319-322.
- [36] Schwierz, Frank. "Graphene transistors." *Nature nanotechnology* 5.7 (2010): 487-496.
- [37] Wang, Xuan, Linjie Zhi, and Klaus Müllen. "Transparent, conductive graphene electrodes for dye-sensitized solar cells." *Nano letters* 8.1 (2008): 323-327.
- [38] Cohen-Tanugi, David, and Jeffrey C. Grossman. "Water desalination across nanoporous graphene." *Nano letters* 12.7 (2012): 3602-3608.
- [39] Gomez De Arco, Lewis, et al. "Continuous, highly flexible, and transparent graphene films by chemical vapor deposition for organic photovoltaics." *ACS nano* 4.5 (2010): 2865-2873.
- [40] Fiorillo M, Verre AF, Iliut M, Peiris-Pagés M, Ozsvari B, Gandara R, Cappello AR, Sotgia F, Vijayaraghavan A, Lisanti MP. Graphene oxide selectively targets cancer stem cells, across multiple tumor types: implications for non-toxic cancer treatment, via "differentiation-based nano-therapy". *Oncotarget*. 2015 Feb 28;6(6):3553-62. doi: 10.18632/oncotarget.3348. PMID: 25708684; PMCID: PMC4414136.
- [41] Stoller, Meryl D., et al. "Graphene-based ultracapacitors." *Nano letters* 8.10 (2008): 3498-3502.
- [42] Lin, Jian, et al. "Laser-induced porous graphene films from commercial polymers." *Nature communications* 5.1 (2014): 1-8.
- [43] Lin, Zhe, et al. "Precise control of the number of layers of graphene by picosecond laser thinning." *Scientific reports* 5.1 (2015): 1-7.
- [44] Bityurin, N., et al. "Models for laser ablation of polymers." *Chemical reviews* 103.2 (2003): 519-552.
- [45] Ramadan, A. A., R. D. Gould, and A. Ashour. "On the Van der Pauw method of resistivity measurements." *Thin Solid Films* 239.2 (1994): 272-275.

- [46] Venkateshalu, Sandhya, et al. "Solvothermal synthesis and electrochemical properties of phase pure pyrite FeS₂ for supercapacitor applications." *Electrochimica Acta* 290 (2018): 378-389.
- [47] Wasterlain, Sébastien, et al. "Hybrid power source with batteries and supercapacitor for vehicle applications." *ESCAP'06* (2006).
- [48] <http://lacey.se/science/eis/>
- [49] <https://zh.m.wikipedia.org/wiki/graphene>
- [50] https://www.researchgate.net/figure/Classification-of-electrolytes-for-electrochemical-supercapacitors_fig4_277894443
- [51] Galiński, Maciej, Andrzej Lewandowski, and Izabela Stępniaik. "Ionic liquids as electrolytes." *Electrochimica acta* 51.26 (2006): 5567-5580.
- [52] Tian, Ying, et al. "Influence of electrolyte concentration and temperature on the capacitance of activated carbon." *Acta Physico-Chimica Sinica* 27.2 (2011): 479-485.
- [53] Fic, Krzysztof, et al. "Novel insight into neutral medium as electrolyte for high-voltage supercapacitors." *Energy & Environmental Science* 5.2 (2012): 5842-5850.
- [54] Demarconnay, L., E. Raymundo-Piñero, and F. Béguin. "A symmetric carbon/carbon supercapacitor operating at 1.6 V by using a neutral aqueous solution." *Electrochemistry Communications* 12.10 (2010): 1275-1278.
- [55] Yang, Hezhen, and Fen Ran. "Progress in Research on Electrolytes for Supercapacitors." (2018).
- [56] Li, Xiangyuan, et al. "Electrochemical Double-Layer Capacitor Containing Mixtures of Ionic Liquid, Lithium Salt, and Organic Solvent as an Electrolyte." *Frontiers in Materials* 8 (2021): 5.
- [57] Sato, Takaya, Gen Masuda, and Kentaro Takagi. "Electrochemical properties of novel ionic liquids for electric double layer capacitor applications." *Electrochimica Acta* 49.21 (2004): 3603-3611.
- [58] <https://www.ceshigo.com/article/10502.html>
- [59] <https://www.researchgate.net/figure/Equivalent-circuit-of-a-supercapacito>
- [60] https://www.researchgate.net/figure/Chemical-structure-of-the-1-butyl-1-methylpyrrolidinium-Pyr-14-and_fig5_340494753
- [61] https://www.researchgate.net/figure/a-Galvanostatic-charge-discharge-curves-measured-with-different-current-densities-for_fig5_275420666
- [62] https://en.wikipedia.org/wiki/Ragone_plot

- [63] Venkateshalu, Sandhya, et al. "Solvothermal synthesis and electrochemical properties of phase pure pyrite FeS₂ for supercapacitor applications." *Electrochimica Acta* 290 (2018): 378-389.
- [64] Szewczyk, Arkadiusz. "Low cost set-up for supercapacitors parameters evaluation." *Journal of Physics: Conference Series*. Vol. 1065. No. 5. IOP Publishing, 2018.